



University of South Florida

## Digital Commons @ University of South Florida

---

USF Tampa Graduate Theses and Dissertations

USF Graduate Theses and Dissertations

---

June 2021

# Low-Cost Device for Laser Phacoemulsification: A Preliminary Study

Mitchell Harrah  
*University of South Florida*

Follow this and additional works at: <https://digitalcommons.usf.edu/etd>



Part of the [Biomedical Engineering and Bioengineering Commons](#)

---

### Scholar Commons Citation

Harrah, Mitchell, "Low-Cost Device for Laser Phacoemulsification: A Preliminary Study" (2021). *USF Tampa Graduate Theses and Dissertations*.  
<https://digitalcommons.usf.edu/etd/9680>

This Thesis is brought to you for free and open access by the USF Graduate Theses and Dissertations at Digital Commons @ University of South Florida. It has been accepted for inclusion in USF Tampa Graduate Theses and Dissertations by an authorized administrator of Digital Commons @ University of South Florida. For more information, please contact [scholarcommons@usf.edu](mailto:scholarcommons@usf.edu).

Low-Cost Device for Laser Phacoemulsification: A Preliminary Study

by

Mitchell Harrah

A thesis submitted in partial fulfillment  
of the requirements for the degree of  
Master of Science in Biomedical Engineering  
Department of Medical Engineering  
College of Engineering  
University of South Florida

Major Professor: Ashwin Parthasarathy, Ph.D.  
Ramesh Ayyala, M.D.  
Christopher Passaglia, Ph.D.

Date of Approval:  
June 21, 2021

Keywords: Phacolysis, Instrumentation, Surgical, Preclinical, Simulation

Copyright © 2021, Mitchell Harrah

## **Dedication**

This thesis is dedicated to the family and friends that have helped and encouraged me throughout my degree. To my mother and sister, thank you for your love and support throughout the last degree, this degree, and the following degree. To my friends throughout my life, thank you for your ongoing encouragement and cheering to keep me going. To TROPICS, thank you for taking a chance on me while being fresh to the field of academic research. Thank you for constantly pushing me to achieve that extra effort both on and off the field to my teams at UF Rugby Football Club and Tampa Krewe Rugby.

## **Acknowledgments**

I want to acknowledge my advisor, Dr. Ashwin Parthasarathy, for offering his guidance and wisdom on approaching the different problems that I ran into throughout this project. I want to acknowledge Abdul Mohaimen Safi for teaching me the basics of COMSOL so that I was able to take advantage of the software entirely. I want to acknowledge Sadhu Moka for helping with the advanced circuitry of this thesis. Finally, I would like to acknowledge my peers at the TROPICS lab for conversing with me when I ran into various issues and teaching me new techniques to overcome them later.

## Table of Contents

List of Tables .....	iii
List of Figures .....	v
Abstract .....	vii
Chapter 1: Introduction .....	1
1.1 Introduction .....	1
1.2 Layout Overview .....	2
1.3 Literature Review .....	3
1.3.1 Review of the Anatomy of a Cataract.....	3
1.3.2 Review of Current Surgical Procedures in Phacolysis .....	4
1.3.2.1 Phacoemulsification.....	4
1.3.2.2 Other Phacolysis Methods .....	5
1.3.3 Review of Finite Element Analysis .....	5
1.4 Objectives .....	6
Chapter 2: Theory .....	7
2.1 Pulsed Lasing .....	7
2.1.1 Introduction.....	7
2.1.2 Ablation.....	7
2.1.3 Thermal Interactions .....	8
2.1.4 Mechanical Interactions.....	11
2.2 Proposed Operation .....	12
Chapter 3: Simulation of Proposed Operation .....	13
3.1 Introduction .....	13
3.2 Materials and Methods .....	13
3.2.1 Anatomical Model of Eye.....	13
3.2.2 Material Properties of Biological Material .....	16
3.2.3 Overview of the Physics Modules .....	19
3.2.4 Overview of the Independent Variables .....	27
3.2.5 Targets of the Dependent Variables.....	29
3.3 Results .....	30
3.3.1 Effects of Power.....	30
3.3.2 Effects of Pulse Width .....	33
3.3.3 Effects on Collimation .....	37
3.4 Conclusion.....	37
Chapter 4: Construction of the Phacolysis Device .....	39

4.1 Considerations for the Device .....	39
4.2 Laser Mount .....	39
4.2.1 Discussion of the Needs of a Custom Design .....	39
4.2.2 Design of the Circuit.....	40
4.2.3 Design of the Outer Shell.....	41
4.2.4 Discussion and Theory on the Addition of Thermal Fins.....	44
4.3 Laser Diode .....	47
Chapter 5: Experimentation on Gelatin .....	49
5.1 Introduction .....	49
5.2 Methods and Materials .....	49
5.2.1 Creation and Analysis of the Gelatin Samples .....	49
5.2.1.1 Phantom Gel Cataract Sample Creation .....	49
5.2.1.2 Survey for Grading .....	51
5.2.1.3 Results of Grading .....	51
5.2.2 Experimental Procedure.....	53
5.3 Results .....	54
5.3.1 Graded Samples Less Than 2.5.....	54
5.3.2 Graded Samples More Than 2.5 .....	58
5.4 Discussion .....	61
Chapter 6: Experimentation on Walnuts.....	63
6.1 Introduction .....	63
6.2 Methods and Materials .....	64
6.3 Results and Discussion.....	65
6.3.1 Continuous Mode.....	67
6.3.2 Ten Millisecond Pulses .....	67
6.3.3 Fifty and Seventy Millisecond Pulses.....	68
6.3.4 Thirty and Ninety Millisecond Pulses.....	69
6.3.5 Discussion of Results.....	69
Chapter 7: Conclusion.....	70
Chapter 8: Future Work .....	71
References.....	72

## List of Tables

Table 2.1: Cataract Lens Material Property Values.....	10
Table 2.2: Calculation of Critical Relaxation Time of Cataract Lens .....	10
Table 2.3: Calculation of Critical Time Constant of Cataract Lens .....	11
Table 3.1: Selected Properties of Ocular Biological Materials.....	17
Table 3.2: Aqueous Humor Material Property Values .....	18
Table 3.3: Cataract Lens Material Property Values.....	19
Table 3.4: Human Blood Property Values .....	22
Table 3.5: Approximate Maximum Temperatures at the Refractive Center of the Human Lens under a Continuous Pulse Width and Laser Radius of 287 $\mu\text{m}$ .....	31
Table 3.6: Approximate Maximum Temperatures at the Refractive Center of the Human Lens under Various Pulse Widths and Laser Radius of 287 $\mu\text{m}$ .....	36
Table 3.7: Tissue Damage at the Refractive Center of the Human Lens under Various Pulse Widths and Laser Radius of 287 $\mu\text{m}$ .....	36
Table 3.8: Maximum Temperature at the Refractive Center of the Human Lens under Various Pulse Widths and Laser Radius of 287 $\mu\text{m}$ .....	37
Table 4.1: Properties of Analyzed Thermal Fins .....	45
Table 4.2: Heat Loss from Single Fin.....	46
Table 4.3: Total Heat Loss from Fin Device .....	47

Table 5.1: Accepted Concentrations from the Survey Performed .....	50
Table 5.2: Statistical Values by the Cataract Sample Survey .....	53
Table 5.3: Area (cm <sup>2</sup> ) of Present Thermal Damage for Formulation A .....	55
Table 5.4: Area (cm <sup>2</sup> ) of Present Thermal Damage for Formulation B.....	56
Table 5.5: Area (cm <sup>2</sup> ) of Present Thermal Damage for Formulation C.....	57
Table 5.6: Area (cm <sup>2</sup> ) of Present Thermal Damage for Formulation D .....	58
Table 5.7: Area (cm <sup>2</sup> ) of Present Thermal Damage for Formulation E.....	59
Table 5.8: Area (cm <sup>2</sup> ) of Present Thermal Damage for Formulation F .....	60
Table 5.9: Area (cm <sup>2</sup> ) of Present Thermal Damage for Formulation G .....	61
Table 6.1: Comparison of Material Property Values .....	63
Table 6.2: Critical Relaxation Time Comparisons .....	64
Table 6.3: Area (cm <sup>2</sup> ) Measurements of Present Thermal Damage with Laser Power at 6750 Milliwatt.....	66

## List of Figures

Figure 3.1: Axisymmetric Slice of the Ocular Model.....	16
Figure 3.2: Temperature of the Refractive Center of the Eye at Laser Radius 287 $\mu\text{m}$ and Laser Power 3000 Milliwatt with No Pulse.....	31
Figure 3.3: Stress Pressure Curve of the Refractive Center of the Eye at Laser Radius 287 $\mu\text{m}$ and Laser Power 3000 Milliwatt with No Pulse.....	32
Figure 3.4: Tissue Damage Curve at the Center of the Anterior and Posterior Cornea at Laser Radius 287 $\mu\text{m}$ and Laser Power 3000 Milliwatt with No Pulse.....	32
Figure 3.5: Temperature Curve at Various Points of the Eye at Laser Radius 287 $\mu\text{m}$ and Laser Power 3000 Milliwatt with No Pulse.....	33
Figure 3.6: The Temperature Curve of the Refractive Center of the Eye at Laser Radius 287 $\mu\text{m}$ and Laser Power 1000 Milliwatt with (A) 10 Millisecond, (B) 30 Millisecond, (C) 50 Millisecond, (D) 70 Millisecond, and (E) 90 Millisecond .....	34
Figure 3.7: The Temperature Curve of the Refractive Center of the Eye at Laser Radius 287 $\mu\text{m}$ and Laser Power 2000 Milliwatt with (A) 10 Millisecond, (B) 30 Millisecond, (C) 50 Millisecond, (D) 70 Millisecond, and (E) 90 Millisecond .....	35
Figure 4.1: Circuit Diagram of the Laser Diode Board .....	41
Figure 4.2: Circuit Diagram of the Thermal Components Board .....	41
Figure 4.3: Interior View from the Bottom View .....	43
Figure 4.4: Side View of Fan and Mount Screw Placements .....	44

Figure 4.5: Prototype Custom Mount (Left) and LDM90/M (Right) Pictured Side by Side .....	44
Figure 5.1: Photograph Scale of the Formulations Used for Gelatin Experiments .....	51
Figure 5.2: LOCS III Classification of Phantom Gel Cataract Samples of Varying Masses Per 750 mL of Water.....	52
Figure 5.3: Area of Thermal Damage on the Surface of Formulation A Gelatins.....	55
Figure 5.4: Area of Thermal Damage on the Surface of Formulation B Gelatins.....	56
Figure 5.5: Area of Thermal Damage on the Surface of Formulation C Gelatins.....	57
Figure 5.6: Area of Thermal Damage on the Surface of Formulation D Gelatins.....	58
Figure 5.7: Area of Thermal Damage on the Surface of Formulation E Gelatins .....	59
Figure 5.8: Area of Thermal Damage on the Surface of Formulation F Gelatins .....	60
Figure 5.9: Area of Thermal Damage on the Surface of Formulation G Gelatins.....	61
Figure 6.1: Measurements of Thermal Damage on the Walnut Surface at 750 Milliwatts of Power .....	66
Figure 6.2: Photograph of Walnuts After Continuous Lasing .....	67
Figure 6.3: Photograph of Walnuts After Ten Milliseconds of Pulsing Width .....	68
Figure 6.4: Photograph of Walnuts After Fifty Milliseconds of Pulsing Width.....	68
Figure 6.5: Photograph of Walnuts After Seventy Milliseconds of Pulsing Width.....	69

## **Abstract**

The current gold standard of cataract removal surgery is phacoemulsification systems. These are divided based on the type of devices used; both are considered equal but with different delivery modes. These delivery methods are either acoustic or light-based. However, these devices pose two hurdles for impoverished areas: high costs and heavy resource usage. This thesis proposes a novel phacoemulsification system is based on the low-cost, off-shelf laser diodes that implement light-based phacoemulsification of cataracts. The system is tested for viability over two methods: finite element analysis and experimentation on various phantoms. Simulations on the device have occurred on the COMSOL software to test the best parameter range for both temperature and pressure within the cataract and tissue damage on the cornea. From this, the most favorable power settings were between 1000 milliwatts and 2000 milliwatts. When working with the experimentation, the media used were gelatin phantoms and walnut kernels. The experiments showed that when the laser was continuously lasing, the liquified or burned areas were much more extensive than when the laser was pulsed. These results show that the device has the possibility of being a viable surgical device, although human cataracts are needed to prove that this device properly works.

## **Chapter 1: Introduction**

### **1.1 Introduction**

From blurry vision to blindness, cataracts are a nuisance to an aging population where cataracts have begun to emerge at a startling rate. For example, in Olmsted County (MN) alone, the incident rate of cataract surgery went from less than 200 per 100,000 persons in 1980 to over 1,000 persons in 2020. While the rates of surgery in the United States are increasing steadily (Erie, Hodge, & Mahr, 2020), most citizens in the United States have a significant advantage since they can easily access the resources to undergo cataract surgery. However, there are some socioeconomic disparities. The ease of access can be attributed to various factors, but these advantages deal with costs and healthcare access (Shahbazi, Studnicki, & Warner-Hillard, 2015).

Even in the United States, there is a significant difference in rural treatment rates compared to urban areas. These differences are amplified in countries like China, India, and Brazil. In 2005, China recorded that around 600,000 cataract surgeries were performed (Tan, 2006). This shocking statistic shows that cataract surgery is not commonly performed on the Chinese population, considering that China contained roughly eighteen percent of the world's entire blind population. Half of that population has cataracts as the leading cause (Tan, 2006). Lack of resources/cost is a fundamental reason why some rural areas cannot meet the glaring demand for much-needed cataract surgery. First, the cost of cataract surgery in these rural areas can range from \$380 to \$1000 in United States currency (Tan, 2006). To some, this may appear to be a low cost. Unfortunately, the minimum price of cataract surgery, which would be more common in a more rural hospital, is almost twice the annual income of those living in a rural area

(Liu, Wilkins, Kim, Malyugin, & Mehta, 2017). This alone would prevent a majority from seeking out cataract surgery, but the lucky few who can afford this cost face even more obstacles. The second obstacle that the rural population faces is the difficulties of transportation (Tan, 2006). In some remote regions, the patients in need of surgery need to find a way to travel several or more miles to reach the closest facility to undergo surgery (Tan, 2006). This only leads to higher costs and burdens to the patient's family and community.

As more impoverished communities gain an aging population, the incident rates of cataracts are going to increase. Furthermore, with costs being well above the annual wages and the communities being comparatively remote to hospitals, the need for a cost-effective and portable method of performing cataract surgery is becoming ever more urgent for these communities. To answer the call for easier access to cataract surgery, this thesis aims to address the beginning steps of developing a low-cost, portable laser-based phacoemulsification device for cataract surgery.

## **1.2 Layout Overview**

This thesis discusses the various theories, analyses, and experiments implemented in constructing a new phacolytic laser. To explain individual pieces coherently for the reader, the thesis is broken down into chapters discussing one relevant topic in depth. These chapters are divided and ordered to help understand the thought process of designing the novel biomedical instrumentation.

Chapter 1 is dedicated to introducing the problem and the current solutions and obstacles currently facing the market. Chapter 2 discusses the various theoretical considerations of developing the phacolytic device. Chapter 3 delves into the simulation steps to verify the likelihood of success and experimental parameters to test. Chapter 4 details the construction and

design of the prototype model utilized in the experiments. Chapters 5 and 6 explore the procedures and results on cataract-simulating gelatin phantoms and walnuts, respectively. Chapter 7 concludes the report with a summary of what was discovered and possible future steps that could be made to improve the device.

## **1.3 Literature Review**

### **1.3.1 Review of the Anatomy of a Cataract**

The human lens is responsible for adequately refracting/focusing light onto the retina of the eye. However, due to the opacity of cataracts, a human lens can no longer appropriately refract light onto the retina. This can result in blurry vision and glares from light, and in severe cases, blindness (Liu, Wilkins, Kim, Malyugin, & Mehta, 2017).

Cataracts are a result of oxidative stress and the layering of proteins in the human lens. Just below the lens capsule, metabolically active epithelial cells are housed to divide into new cells and produce insoluble proteins called crystallins. Unfortunately, as the cells begin to lose their metabolic activity, the old cells start to congregate in the center of the lens to form lens fibers, which eventually leads to a decrease in the diffusion of water and other required metabolic species (Pescosolido, Barbato, Giannotti, Komaiha, & Lenarduzzi, 2016). With the decrease of water transportation into the lens, the crystallins become dehydrated and begin the aggregation that begins the cataract process (Pescosolido, Barbato, Giannotti, Komaiha, & Lenarduzzi, 2016). As more metabolically inactive cells begin moving into the center, the cells and proteins become highly concentrated, resulting in a solid core called the nucleus. As the cataract becomes worse, the nucleus begins to grow as well. Interestingly, the cataract shows a gradient of opacity since the older cells slowly congregate into the nucleus (Liu, Wilkins, Kim, Malyugin, & Mehta, 2017).

### 1.3.2 Review of Current Surgical Procedures in Phacolysis

Phacolysis, or the surgical procedure of removing a cataract, has undergone quite a few changes throughout medical history. However, the current trends in the procedure are the focus of this section. Most techniques used in the United States involve phacoemulsification via ultrasound or a femtosecond laser. Although, in some areas of the world, intracapsular cataract extraction and extra capsular cataract extraction are used.

#### *1.3.2.1 Phacoemulsification*

Phacoemulsification is widely used in countries like the United States and is considered the gold standard of cataract surgery procedures. The procedure is simplified in broad steps. First, the surgeon makes a small incision in the anterior surface of the lens capsule. Then, a phacoemulsification device is introduced into the eye through the incision. The device then emulsifies the cataract. This means that the device essentially turns the cataract into a liquid that is turned into a homogenous mixture with the remaining media of the lens. The emulsion is then extracted from the lens and replaced with an intraocular lens. Overall, the procedure is successful in treating the cataract. Multiple reports concluded that visual outcomes in patients improved a noticeable amount. Another benefit of this surgery method is that the recovery period is significantly shorter and more successful than previously utilized methods (Donaldson, et al., 2013).

Phacoemulsification has multiple variations of the process. The two popular variations revolve around the ultrasound method and the femtosecond laser method. The ultrasound method relies on a probe that applies rapid sonic vibrations to emulsify the cataract. On the contrary, the femtosecond laser relies on utilizing a series of quick pulses to apply photo-thermal stresses to emulsify the cataract. Though these methods provide no statistically significant difference in the

procedure results, the equipment utilized for both is very costly in both initial and recurring costs. Unfortunately, most rural hospitals in developed countries cannot afford the equipment. Furthermore, if they could afford it, the equipment is not portable, making those in distant communities expend further costs for transportation (Donaldson, et al., 2013).

#### *1.3.2.2 Other Phacolysis Methods*

With high costs and low accessibility, many rural areas of developing countries have resorted to outdated techniques of intracapsular cataract extraction and extracapsular cataract extraction. First, intracapsular cataract extraction removes the entire lens capsule and parts of the surrounding (Ruit, Tabin, Nissman, Paudyal, & Gurung, 1999). Unfortunately, this leads to multiple complications both during and after surgery. Extracapsular cataract extraction works similarly to phacoemulsification except that the cataract is removed as a solid and not emulsified (Donaldson, et al., 2013). This results in larger incisions in the eye and a high occurrence of astigmatism, or blurry vision, after the surgery (Ruit, Tabin, Nissman, Paudyal, & Gurung, 1999). With the high amounts of complications of these outdated procedures, a low-cost, portable solution could answer the vast health disparities of the rural communities of developing nations.

#### 1.3.3 Review of Finite Element Analysis

The human eye has a vast amount of various physical components and functions that are affected during phacolysis. From the flow of the aqueous humor to the stress pressure that the lens might experience, there are numerous factors and relationships to calculate that are inconceivable for one person to do by hand. Also, experimentation can be costly and time-consuming. With finite element analysis, a computer can rapidly calculate the effects that the human eye may undergo during a surgery utilizing the prototype phacolysis device. With the

massively reduced time of calculation, multiple variables can be tested to seek the overall efficacy of the proposed procedures.

As strides in computing have advanced science, various applications have been released to the scientific community. One of the most popular applications is COMSOL. COMSOL can create geometries that can represent various structures, including ocular structures. From heat transfer to fluid flow, the program can calculate the physical interactions seen during the procedure. The University of South Florida currently provides a computing tool to the researchers to help the university's computing community solve even the most daunting problems.

#### **1.4 Objectives**

As previously stated, the objective is to create a low-cost and highly accessible phacolysis device that can be used to treat patients in rural communities in developing countries. However, the device must be comparable to the current gold standard of phacoemulsification. By creating a similar device with convenience to these communities, the populace of these communities will experience a higher quality of life after the surgery. To accomplish this ultimate objective, a finite element analysis model will be built to test the efficacy of the proposed device and procedure. While testing the simulation, a set of variables will be selected from the results that show the most promise of the best route of care. Finally, the prototype will be tested on cataracts simulating gelatin phantoms and walnuts to see if the prototype will treat the cataract. The preliminary results derived from this study will form the basis for controlled future experiments in *ex-vivo* cataracts from cadavers and eventually human subject clinical trials.

## Chapter 2: Theory

### 2.1 Pulsed Lasing

#### 2.1.1 Introduction

Unfortunately, ultrasound and femtosecond laser setups are expensive and hefty and consume a vast amount of space. These setups go against the two significant goals of this project: portability and cost-effectiveness. However, the femtosecond laser does lead to the inspiration for the proposed technology. With this thesis, the microsecond pulsed laser is tested to evaluate the efficacy of bursting a cataract of various classes according to the Lens Opacities Classification System III.

The proposed millisecond pulsed laser offers a few benefits as a solution. First, the specifications for operation do not require a significant number of resources, which will help when working in remote areas where a robust electrical grid may not be present and provide a path to creating the device cheaply in a manufacturing setting. Second, the proposed millisecond pulsed laser does not require ample space to house the equipment. The overall portability can provide a physician to easily store and move the setup to a residence in remote or rural areas. Lastly, the millisecond laser is inspired by the femtosecond laser. This means that the idea of pulsing the laser is not novel, but the alterations in operation parameters and implementing a diode rather than a crystal provide substantial differences.

#### 2.1.2 Ablation

In both the femtosecond and millisecond laser, the primary mechanism of phacoemulsification is ablation. Ablation is the process that occurs when the surface of a solid

material erupts due to a short laser pulse width, or laser pulse duration, with a high-powered setting (Sun, Han, Niemz, & Bille, 2007). This happens when the material's surface is heated beyond its vaporization temperature within a fraction of the laser pulse width. More formally, ablation occurs when the fluence, or the energy deposited in the illuminated area, surpasses the ablation threshold within a set pulse width (Sun, Han, Niemz, & Bille, 2007).

Typically, ablation is seen with laser pulse widths within the nanoseconds range rather than the millisecond range (Sun, Han, Niemz, & Bille, 2007). When working with a femtosecond laser on the corneal tissue, the performing researchers noticed an exponential rise of the ablation threshold requirements as the pulse width increased (Sun, Han, Niemz, & Bille, 2007). This could provide a potential hurdle as the millisecond pulse width has a more extended pulse width than a femtosecond laser. However, this apparent limitation is answered in both the collimation design and the peak power of the laser. First, the collimation design alters the area of illumination, which is where the power of the laser is deposited. Currently, there are two collimation designs of interest for this project. The first collimation has a laser radius of 287 micrometers. The second collimation design has a much smaller radius of 750 nanometers. This alone could already solve the ablation issue with the millisecond, but the designed laser can perform up to three watts of power. With the combination of the collimation designs and the high-powered laser, the ablation threshold could be achieved on the millisecond pulse width. However, to see if this is physically achievable, ablation's thermal and mechanical interactions must be studied.

### 2.1.3 Thermal Interactions

When working with a pulsed laser, the thermal interactions with the material are crucial to understanding what may happen during the heating process. The critical component of the

thermal interaction is how the heat may propagate in the material when the laser is pulsed. Utilizing the physics of pulsing lasers and heat transfer, if the pulses are short, the heat stays concentrated to the illuminated area before eventually propagating to its surroundings (Jacques, 1992). However, if the pulse width is considered long, the material has enough time to properly propagate heat across its surroundings (Jacques, 1992).

Now, the boundary between a short and long pulse needs to be defined to adjust our testing parameters accurately. To accomplish this objective, the critical relaxation time formula is used. The formula is defined as (Jacques, 1992),

$$t_r = \frac{(2*\delta)^2}{\kappa} \quad (\text{Eq. 2.1})$$

In this equation, the thermal diffusivity in squared centimeters per second noted as  $\kappa$ , and the penetration depth in centimeters noted as  $\delta$  is used to find the critical relaxation time, shown as  $t_r$ , in units of seconds. When utilizing the critical relaxation time, the classification of the laser pulse width is simple. If the laser pulse width is less than the critical relaxation time, the pulse width is short, and the heat remains concentrated (Jacques, 1992). Conversely, when the laser pulse width is greater than the critical relaxation time, the pulse width is long, and the heat can propagate heat across the material's surroundings. The function for the penetration depth and thermal diffusivity needs to be defined and calculated to find the critical relaxation time for the cataract lens.

First, the penetration depth function is defined as (Jacques, 1992),

$$\delta = \frac{1}{\sqrt{3*\mu_a*(\mu_a+\mu'_s)}} \quad (\text{Eq. 2.2})$$

As the function shows, the penetration depth depends on the absorption of the material ( $\mu_a$ ) and reduced scattering ( $\mu'_s$ ) coefficients. Thermal diffusivity is simply noted as (Jacques, 1992),

$$\kappa = \frac{K}{C_p * \rho} \quad (\text{Eq 2.3})$$

The thermal diffusivity function shows that the thermal diffusivity relies on the thermal conductivity, K, as Watts per meter per Kelvin, the heat capacity at constant pressure, C<sub>p</sub>, as Joules per kilogram per Kelvin, and the density, ρ, as kilograms per cubed meter.

The material properties of the cataract lens are required to solve for the critical relaxation time are listed in Table 2.1 below.

Table 2.1: Cataract Lens Material Property Values

Property (Units)	Value
Density (kg/m <sup>3</sup> )	1000
Thermal Conductivity (W/(m*K))	0.4
Specific Heat (J/(kg*K))	3000
Absorption Coefficient (1/cm)	10
Reduced Scattering Coefficient (1/cm)	20

Table 2.2 shows the results for the penetration depth, thermal diffusivity, and critical relaxation time given the values of the required parameters and the equations above.

Table 2.2: Calculation of Critical Relaxation Time of Cataract Lens

Property (Units)	Value
Penetration Depth (cm)	0.03
Thermal Diffusivity (cm <sup>2</sup> /s)	0.0013
Critical Relaxation Time (s)	0.83

Looking at Table 2.2, about 833 milliseconds are needed to reach a long pulse width. Given that the millisecond laser is seeking to provide pulse width below 100 milliseconds to avoid large fluence values, the millisecond pulsed laser should still be physically capable of achieving ablation, at least thermally.

#### 2.1.4 Mechanical Interactions

Like the thermal interactions, mechanical interactions are vital to understanding whether ablation can occur in the cataract. To ensure that the cataract can properly break apart into smaller pieces, the mechanical stress must stay in a concentrated area to help ablation. The short pulse width helps concentrate the mechanical stress to the illuminated area (Jacques, 1992).

Extended pulse widths then propagate the mechanical stress across the material (Jacques, 1992).

To find if the laser pulse is within the ideal range, another time constant needs to be calculated to determine the boundary condition to determine the pulse width limit before stress propagates.

To solve for the mechanical interaction, the critical time constant needs to be defined.

The equation that is used is (Jacques, 1992),

$$t_0 = \frac{\delta}{v} \quad (\text{Eq 2.4})$$

The equation shows that, once again, the penetration depth is used in conjunction with the speed of sound in the tissue, shown as  $v$ . The speed of sound inside of human tissue is 1500 meters per second for calculating the critical time constant (Jacques, 1992). Given that the penetration depth was calculated in the previous section, the critical time constant can be solved. Table 2.3 gives the critical time constant with the penetration depth and speed of sound values used.

Table 2.3: Calculation of Critical Time Constant of  
Cataract Lens

Property (Units)	Value
Penetration Depth (cm)	0.03
Velocity of Sound in Tissue (m/s)	1500.00
Critical Time Constant ( $\mu\text{s}$ )	0.22

Unfortunately, the critical time constant does not indicate that the mechanical interactions do not help with the ablation of the cataract. However, the thermal interactions may be enough to provide for the breakdown of the cataract. In the following few chapters, simulations and

experimentation is performed to verify whether the mathematics provided were close and accurate.

## **2.2 Proposed Operation**

Before moving on to simulations and experimentation, the operation of the device should be discussed quickly. To begin, a small optical fiber will be inserted in the lateral side of the sclera via a small incision. The fiber will then provide a short laser pulse to create a small gap to enter the lens capsule. The laser fiber will then be placed close above the cataract nucleus. The laser will then pulsate to induce the thermal and mechanical changes to the material. This will proceed for a total of ten seconds.

Once the operation is completed, the cataract is then removed via a small vacuum probe. When the discarded material is removed, the physician will reseal the incisions. This will then signal the end of the operation. As the experimentations are further implemented, the proposed operation will change as needed to provide the best route of care to future patients.

## **Chapter 3: Simulation of Proposed Operation**

### **3.1 Introduction**

Computer simulations are an integral part of testing the preliminary idea of a biomedical device. These simulations are used to determine the designs of the device and how the device may operate. In this case, ensuring that thermal damage is avoided is the primary outcome measure for the simulations. Further, by taking the time to design and analyze simulations, experimentation can be significantly reduced by looking at specifically chosen parameters that passed the simulations' key objectives. In this simulation, COMSOL Multiphysics 5.5 was used to analyze further the behaviors and trends observed in the ocular space when the millisecond phacolytic laser utilizes various laser settings.

### **3.2 Materials and Methods**

#### **3.2.1 Anatomical Model of Eye**

To simulate the device on the human eye, a model of the eye had to be created to test it correctly. For this, the paper, “Anatomically Accurate, Finite Model Eye for Optical Modeling,” was used as the primary source to design the human eye (Liou & Brennan, 1997). The simulation requires the cornea, lens, sclera, iris, aqueous humor, and vitreous humor to visualize the surgical procedure's effects properly. While building the eye model, the goal is to construct the eye as if a patient were laying down on their back, looking up towards the ceiling. Further, the refractive center, or the point in the eye where the refractive index for the anterior and posterior curves are equal, is considered the origin of this model.

The construction of the eye requires curves for three of the solid structures. To accomplish for two of the structures, the cornea and lens, the equation,

$$x^2 + y^2 + (1 + Q) * z^2 - 2 * z * R = 0, \quad (\text{Eq. 3.1})$$

where Q represents the asphericity, which is unitless, and R represents the radius of the curve, which is in millimeters. For the construction of the eye model, the shape was built as a two-dimensional axisymmetric model. This means that a model is built on a two-dimensional plane that is then rotated around a central plane axis to create a three-dimensional geometry. Because the two-dimensional axisymmetric model is used, the coordinate plane is in a cylindrical coordinate plane rather than a Cartesian coordinate plane. Since cylindrical coordinates are used, the equation used to plot the curve must be adjusted. Using the quick conversion of

$$x^2 + y^2 = r^2, \quad (\text{Eq 3.2})$$

the new equation of plotting the curves in COMSOL is now,

$$r^2 + (1 + Q) * z^2 - 2 * z * R = 0. \quad (\text{Eq 3.3})$$

Further, when discussing the placement and construction of the curve, the tip's orientation and placement must be discussed. In most cases, the curve is positively orientated, or where the tip of the curve is the highest point. However, in one particular case, the curve is negatively orientated, or where the tip of the curve is the lowest point.

To begin, the lens of the eye has an exciting and unique shape. There is a shallow curve on the anterior side with the tip of the curve less than two millimeters away from the refractive center of the lens. This is contrasted from the posterior curve of the lens with a deeper, more circular curve with the tip over two millimeters away from the refractive center. This means that their asphericity and radius are different from each other. For the anterior curve, the parameters are that the asphericity is -0.94 and the radius is 12.40 millimeters. The anterior curve is also

positively orientated, and the tip of the curve is at 1.59 millimeters. For the posterior curve, the parameters are that asphericity is 0.96 and the radius is -8.10 millimeters. The posterior curve is negatively orientated, and the tip of the curve is at -2.59 millimeters. The curves were drawn to meet at the point (5.4794, 0.3758) in coordinate point form (r, z).

Next, the cornea is the following structure that must be built using Equation 3.3. Here, both curves are positively orientated, but they differ in both asphericity and radius. For the anterior corneal curve, the asphericity is -0.18, the radius is 7.77 millimeters, and the tip of the curve is at 5.19 millimeters. However, the posterior corneal curve has an asphericity of -0.60, a radius of 6.40, and a tip placement at 4.64 millimeters. When the curves are built, the end point of the anterior curve is at (5.9517, 2.53998) and the posterior curve is at (5.9517, 1.57998). Here, the distance of the two start points is .5 millimeters, and the two end points have .96 millimeters, which is five percent more than the value recorded in the source paper.

With developing the sclera, the model assumes that it is a perfect sphere for both the posterior and anterior curves while ignoring the fovea structure that appears like a small dent. It is also assumed to remain at a constant thickness of 0.96 millimeters for the sclera due to the ending thickness of the cornea. In COMSOL, the 'Circle' geometry option was used to create the two boundaries. The center of both circles was at the position (0, -6.43398). Both circles were rotated at negative ninety degrees. The radius of the posterior circle was 9.98 millimeters, and the sector angle of the circle was set at 143.40 degrees. The anterior circle was constructed differently with a radius of 10.77 millimeters, and the sector angle was 146.45 degrees. By building the circles under these conditions, the sclera should be connected to the cornea and end at the axis of rotation.

Finally, the construction of the iris was simplified due to two reasons. First, the iris was used as a boundary to separate the eye's aqueous and vitreous humor fluids. Second, the iris does not have a clearly defined shape that would affect the surgery for photolysis since it would be moved away from the cataract during operation. Because of this, the iris was built to have a maximum thickness of 0.46 millimeters (Lee, et al., 2014). The iris was built using the polygon geometry with a starting and ending point where the posterior cornea and sclera curves intersect.

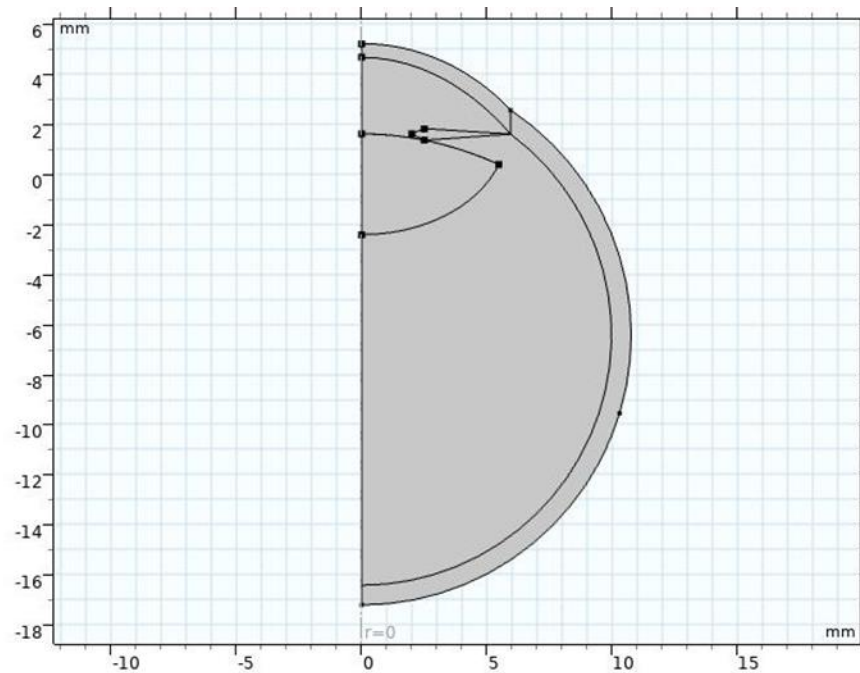


Figure 3.1: Axisymmetric Slice of the Ocular Model

### 3.2.2 Material Properties of Biological Material

To create a realistic model, material properties are just as important as the geometry that was built in the previous section. For all materials, the density, thermal conductivity, and heat capacity at constant pressure were necessary properties that were needed to be defined. However, the lens had a thermal conductivity that was dependent on the temperature. This is also true for the density of the aqueous humor, as it changed due to temperature changes. Table 3.1 shows the constant values of density, thermal conductivity, and heat capacity at constant pressure for the

biological material (Mirnezami, Jafarabadi, & Abrishami, Temperature Distribution Simulation of the Human Eye Exposed to Laser Radiation, 2013). The temperature-dependent equations are discussed in this section.

Table 3.1: Selected Properties of Ocular Biological Materials

Material	Density (kg/m <sup>3</sup> )	Thermal Conductivity (W/(m*K))	Heat Capacity at Constant Pressure (J/(kg*K))
Cornea	1050	0.58	3500
Aqueous Humor	Eq 3.4	0.58	4200
Lens	1050	0.40	4200
Vitreous Humor	1050	0.603	4200
Sclera	1050	1.0042	3500
Iris	1050	1.0042	3500

Two biological materials need to be further expanded. The aqueous humor will undergo hydrodynamic physics, which requires other properties and the equation for the changing density to be defined. The lens will experience heating via a laser mechanism and possible thermal expansion due to the breaking of cataract solids. This will require different material properties to be expanded and the equation for changing thermal conductivity to be shown.

First, the aqueous humor has a density that changes the temperature changes (Ooi & Ng, 2008). To create this effect, COMSOL allows the user to input equations into the material properties to reflect the temperature dependency. The equation used for this is (Ooi & Ng, 2008),

$$\rho = \rho_0 * [1 - \beta * (T - T_0)] \quad (\text{Eq. 3.4})$$

Here,  $\rho_0$  represents the reference density as kilograms per cubic meters,  $\beta$  shows the volume expansion coefficient as inverted Kelvins, and  $T_0$  is the reference temperature in Celsius. For the

aqueous humor, the reference density is 996 kg/m<sup>3</sup>, the volume expansion coefficient is 0.0003 K<sup>-1</sup>, and the reference temperature is 34 °C (Ooi & Ng, 2008). Further, the dynamic viscosity and specific heat ratio must be defined in COMSOL to perform the fluid dynamic physics. The aqueous humor has a dynamic viscosity of 0.00074 N\*s/m<sup>2</sup> and a specific heat ratio of 1.66 (Ooi & Ng, 2008). The specific heat ratio of the aqueous humor in this paper is identical to that of water due to the close similarity of the two fluids. Table 3.2 shows the summary of the extra values that have been noted for the aqueous humor.

Table 3.2: Aqueous Humor Material Property Values

Property (Units)	Value
Reference Density (kg/m <sup>3</sup> )	996
Volume Expansion Coefficient (K <sup>-1</sup> )	0.0003
Reference Temperature (°C)	34
Dynamic Viscosity (N*s/m <sup>2</sup> )	0.00074
Specific Heat Ratio (1)	1.66

For the lens properties, the heating through the laser and the mechanical stresses are to be considered. First, the heating through the laser only requires the absorption coefficient as it decides how much laser energy is transferred into the material. The absorption coefficient is dependent on the wavelength of the laser and the classification of the cataract lens. Usually, when the classification of the cataract lens is higher, the absorption coefficient differences become more prominent as well. However, the absorption coefficients for all classifications are all within 10 cm<sup>-1</sup> for the wavelength of 1485 nm (Belikov, et al., 2019). So, the absorption coefficient used for the simulation for the cataract lens is 10 cm<sup>-1</sup>. Next, the lens will undergo mechanical stress due to the heating of the material. For COMSOL to perform the mathematics,

it requires that the lens has a defined Young’s modulus, Poisson’s ratio, and coefficient of thermal expansion. The parameters for this are 6000 kPa for the Young’s modulus, 0.47 for Poisson’s ratio, and  $0.0003 \text{ K}^{-1}$  for the coefficient of thermal expansion (Fisher, 1969). The coefficient of thermal expansion for both the lens and aqueous humor is the same in the simulation due to the close similarity to fluid components of each to that of water at  $32 \text{ }^\circ\text{C}$ . Table 3.3 shows the summary of the extra values that have been noted for the cataract lens.

**Table 3.3: Cataract Lens Material Property Values**

Property (Units)	Value
Absorption Coefficient (1/cm)	10
Young's Modulus (kPa)	6000
Poisson's Ratio (1)	0.47
Volume Expansion Coefficient ( $\text{K}^{-1}$ )	0.0003

### 3.2.3 Overview of the Physics Modules

For the simulation, seven physics modules were utilized to give a realistic model to the phacolysis surgery. These modules were Bioheat Transfer, Laminar Flow, Nonisothermal Flow, Radiative Beam in Absorbing Media, Heat Transfer with Radiative Beam in Absorbing Media, Solid Mechanics, and Thermal Expansion. For Nonisothermal Flow, Heat Transfer with Radiative Beam in Absorbing Media, and Thermal Expansion, the modules are considered Multiphysics modules and rely on two or more physics modules to help provide a more realistic relationship to different phenomena. For this section, the modules will be broken down to understand what parameters COMSOL is requesting and the equation that COMSOL utilizes to provide a model that can be investigated. The source for these explanations is the COMSOL Help Handbook (COMSOL, 2021).

First, the Bioheat Transfer module will be discussed as it is the primary module used for this study. In COMSOL, the equation that the software uses is,

$$\rho * C_p * \frac{\partial T}{\partial t} + \rho * C_p * \mathbf{u} \cdot \nabla T + \nabla \cdot \mathbf{q} = Q + Q_{bio} + Q_{vd} \quad (\text{Eq 3.5})$$

To further understand the equation, it will be broken down by the different terms, each in Joules per second per cubic meter, where it can be explained easier. The first term,  $\rho * C_p * \frac{\partial T}{\partial t}$ , denotes the rate of change over time of the internal energy of the biological media. Here,  $\rho$  is the density of the biological media as kilograms per cubed meters,  $C_p$  is the heat capacity at constant pressure as Joules per meter per Kelvin,  $T$  a function of temperature with respect to time, and  $t$  is representative of time. The second term,  $\rho * C_p * \mathbf{u} \cdot \nabla T$ , represents the convective heat transfer of the fluidic biological media. This is because  $\mathbf{u}$  is the velocity field, in units of meters per second, and will only be applied to fluid-based biological media, such as the aqueous humor. The velocity field will be discussed in more detail in the Laminar Flow and Nonisothermal Flow modules. The final term of the left-hand side of the equation,  $\nabla \cdot \mathbf{q}$ , is the conductive heat transfer of the biological media. In this equation,  $\mathbf{q}$  is called the heat flux as Watts per squared meters and is defined by the equation,

$$\mathbf{q} = -k\nabla T \quad (\text{Eq 3.6})$$

In Eq 3.6, the thermal conductivity is denoted by the letter  $k$  in units of Watts per meter per Kelvin. However, this equation does change at the anterior boundaries of the cornea and sclera since they are both exposed to the surrounding air. In this case,

$$-k\nabla T = h(T_{ext} - T) \quad (\text{Eq 3.7}),$$

where the heat transfer coefficient is shown as  $h$  in units of Watts per squared meters per Kelvin. For this simulation, the heat transfer coefficient is  $10 \text{ W}/(\text{m}^2 \cdot \text{K})$ , and the external temperature is  $25 \text{ }^\circ\text{C}$ .

Finally, on the right-hand side, the heat generation term shows up as the summation of  $Q$ ,  $Q_{bio}$ , and  $Q_{vd}$ , which are the source of heat generation, the biological heat generation, and heat generation by viscous dissipation, which will be discussed in more detail in the Nonisothermal Flow module. For the source heat generation, laser heating will take over this portion of the variable. This will be discussed further in the Heat Transfer with Radiative Beam in Absorbing Media module later in this section. Biological heat generation is the heat generation created by blood flow and the body's metabolic processes. This heat generation model is described in the equation,

$$Q_{bio} = \rho_{blood} * C_{p,blood} * \omega_{blood} * (T_{blood} - T) + Q_{metabolic} \quad (\text{Eq 3.8})$$

The blood perfusion rate, denoted by  $\omega_{blood}$ , is the rate, as inversed seconds, that arterial blood is delivered to the capillary beds of the biological tissue of interest. However, the lens and cornea do not have any blood flow through them or have any metabolic processes ongoing in their boundaries. Because of this, the sclera and iris are the only structures with biological heat generation. In this case, the density of blood was equal to  $1060 \text{ kg/m}^3$ , the heat capacity was equal to  $3594 \text{ J/(kg} \cdot \text{°C)}$ , the blood perfusion rate was  $35000 \text{ s}^{-1}$ , the temperature of blood was  $37 \text{ °C}$ , and the metabolic heat generation was  $1000 \text{ W/m}^3$  (Mirnezami, Jafarabadi, & Abrishami, Temperature Distribution Simulation of the Human Eye Exposed to Laser Radiation, 2013). Table 3.4 summarizes the values given for ease of reading.

Property (Units)	Value
Density (kg/m <sup>3</sup> )	1060
Heat Capacity at Constant Pressure (J/(kg*K))	3594
Blood Perfusion Rate (s <sup>-1</sup> )	35000
Temperature (°C)	37
Metabolic Rate (W/m <sup>3</sup> )	1000

The final portion of the Bioheat Module is the Tissue Damage modeling for the corneal tissue. For the simulation, a temperature threshold model with hyperthermia analysis is used. The equation is simply,

$$\frac{\partial \alpha}{\partial t} = \frac{1}{t_{d,h}} (T > T_{d,h}) \quad (\text{Eq 3.9})$$

This means that, as the temperature is above the specified damage temperature, damage to the tissue will occur over time until fully damaged at the noted damage time. For this case, the damage temperature is 59 °C, and the damage time is 60 sec (Wirbelauer, et al., 2000). Further, if the corneal tissue reaches 65 °C, the heated corneal tissue will be rendered destroyed (Wirbelauer, et al., 2000).

The next module that will be discussed is the Laminar Flow module. The Laminar Flow module was chosen for this simulation to help model the convective heat flow present with the aqueous humor region of the eye. The output of this module is the velocity field, which is used for the aqueous humor region in the Bioheat module. The momentum equation that COMSOL uses is,

$$\rho * \frac{\partial \mathbf{u2}}{\partial t} + \rho * (\mathbf{u2} \cdot \nabla) * \mathbf{u2} = \nabla \cdot [-p * \mathbf{I} + \mathbf{K}] + \mathbf{F} + \rho \mathbf{g} \quad (\text{Eq 3.10})$$

COMSOL derives this equation by using the continuity equation,

$$\frac{\partial \rho}{\partial t} + \nabla \cdot (\rho * \mathbf{u2}) = 0 \quad (\text{Eq 3.11})$$

To understand this equation, the individual terms will be discussed briefly. The first term describes the acceleration over time. In this equation,  $\mathbf{u2}$  is the output velocity of the module as meters per second. The second term shows the convective acceleration of the fluid. The right-hand side of the equation is the summation of the various forces that the fluid undergoes. Within the first section,  $-p*\mathbf{I}$  is the pressure tensor, which means  $p$  is pressure, at Newtons per squared meters, and  $\mathbf{I}$  is the identity tensor. Since this portion is working with the aqueous humor region of the eye, intraocular pressure will need to be described. The intraocular pressure will be defined as 15 mmHg for the simulation (Ooi & Ng, 2008). A pressure point needs to be defined, which is along the cornea's posterior curve. The following tensor, noted as  $\mathbf{K}$ , is the stress tensor. The stress tensor is written as

$$\mathbf{K} = \mu * (\nabla \mathbf{u2} + (\nabla \mathbf{u2})^T) - \frac{2}{3} \mu * (\nabla \cdot \mathbf{u2}) * \mathbf{I} \quad (\text{Eq 3.12})$$

For this equation, the T does not mean temperature but indicates that the tensor is transposed. The symbol,  $\mu$ , denotes that COMSOL searches for the dynamic viscosity, as Pascal times seconds. The next part of the summation of the volumetric forces is the term  $\mathbf{F}$ , or the summation of forces that are not related to pressure, viscous, or gravitational forces. The only force that is of interest is the buoyancy forces due to the changing of the fluid density, which is already considered by the changing density. Finally, the gravitational forces are defined last. For this term, a gravity node is added to indicate that gravity is directed towards the negative z-direction.

As the lens's temperature is heated, the aqueous humor touching the boundary is also heated. However, as the aqueous humor becomes at a higher temperature, the fluid density is decreased. This phenomenon results in a buoyancy force with the lighter density portion of the

fluid moving against gravity as the cooler, heavier fluid moves with gravity. Unfortunately, the Laminar Flow module does not account for the changing of the densities, so the Nonisothermal Flow module is added to the simulation. The module accounts for the changing of the densities and the heat generated by viscous dissipation, or  $Q_{vd}$  from the Bioheat Module. However, due to the low velocities of the fluid, the heat generation in this module is neglected to conserve computing resources.

The Radiative Beam in Absorbing Media and Heat Transfer with Radiative Beam in Absorbing Media modules are used for the next set of modules. To begin, the Heat Transfer with Radiative Beam in Absorbing Media only uses one equation to define a heat generation term. This term is the primary heat generation method through the Bioheat module. The equation that is defined is,

$$Q = \sum_i \kappa I_i \quad (\text{Eq 3.13})$$

The equation is simply the summation of the products of the absorption coefficient,  $\kappa$ , and the incident intensities. However, this simulation only requires one beam, which helps reduce calculation times.

Now, the incident intensity must be defined to compute the heat generation. The Radiative Beam in Absorbing Media module helps in conjunction with the Heat Transfer with Radiative Beam in Absorbing Media module. COMSOL utilizes the equation,

$$\frac{e_i}{\|e_i\|} \cdot \nabla I_i = -\kappa * I_i \quad (\text{Eq 3.14})$$

to help define the relationship between incident intensity, absorption coefficient, and beam orientation. The module goes further to ensure that the beam is properly defined. Under the Incident Intensity section of the module, various inputs are needed to help COMSOL understand the beam. These inputs are the orientation and profile, which includes power, origin point, and

distribution method. For the simulation, the orientation is only in the negative direction along the z-axis, and the origin point of the beam is at .585 millimeters, as explained in the Theory chapter in the Purposed Operation section. As for the distribution method, the Top-Hat Method was chosen due to the configuration of the diode used for the experimentation, which is furthered explain in the Construction of Phacolysis Laser chapter. The change of radius was set as zero to assume an ideal beam. These are considered the independent testing variables with power and the beam radius and are discussed in the next section. With the new parameters, COMSOL can calculate the incident intensity with the equation,

$$I_i = P_0 \cdot f(\mathbf{O}, \mathbf{e}) * \frac{|\mathbf{e} \cdot \mathbf{n}|}{\|\mathbf{e}\|} \quad (\text{Eq 3.15})$$

In the equation,  $P_0$  is the deposited beam power, the positional illumination is denoted as the function  $f$ ,  $\mathbf{e}$  is the beam orientation,  $\mathbf{O}$  is the beam position, and  $\mathbf{n}$  is the normal vector of the surface where the beam will impact. Further, the function of the positional illumination is needed to find the incident intensity. The positional illumination function changes based on the distribution method, which, as previously stated, is the Top-Hat Method. The function provided by the Top-Hat Method is,

$$f(\mathbf{O}, \mathbf{e}) = \begin{cases} \frac{1}{\pi * R^2}, & \text{if } d \leq R \\ 0, & \text{if } d > R \end{cases}, \quad d = \frac{\|\mathbf{e} \times (\mathbf{x} - \mathbf{O})\|}{\|\mathbf{e}\|} \quad (\text{Eq 3.16})$$

In this equation, the variables used that have not been previously recorded are radius and position on the cylindrical coordinate plane. These values are shown as  $R$  and  $\mathbf{x}$ , respectively.

Finally, the boundaries of the Radiative Beam module must be defined. The Incident Intensity boundary is at the center of the anterior curve of the lens. The remaining portion of the anterior lens and the posterior curve are defined as Transparent Surfaces. This is because that

although the media has some cloudiness, light can still pass through the boundary with relative ease.

The final group of modules that are discussed is the Solid Mechanics and Thermal Expansion modules. Unlike the previous modules, these modules are not required to help define the Bioheat Module. Instead, the Bioheat Module helps feed information into these modules so that the internal pressure of the lens can be monitored. Though the equations may be complex, this module has been significantly simplified to only monitor the effects of the strain by thermal expansion. The central equation for the Solid Mechanics module is,

$$0 = \nabla \cdot \mathbf{S} + F_V \quad (\text{Eq 3.17})$$

The equation shows that the summation of the divergence of the stress and the volume forces are equal to zero. For the simplicity of the equation,  $F_V$ , or the volume forces, is equal to zero due to that the lens will be suspended freely within the eye.

To define the divergence, the type of material that the lens acts as must be defined. The Linear Elastic Material node was chosen as it was best suited from prior research. For the stress tensor, COMSOL gives a series of equations that are needed to solve the stress tensor equation,

$$\mathbf{S} = \mathbf{S}_{ad} + \mathbf{C} : \boldsymbol{\epsilon}_{el} \quad (\text{Eq 3.18})$$

Because there are no defined initial or external forces in the simulation, the added stress tensor, or  $\mathbf{S}_{ad}$ , equals zero. However, the term with the stiffness matrix and elastic strain tensor is further defined.

First, the displacement strain tensor is needed. This is defined as,

$$\boldsymbol{\epsilon} = \frac{1}{2} [(\nabla * \mathbf{u})^T + \nabla * \mathbf{u}] \quad (\text{Eq 3.19})$$

The equation utilizes the displacement vector  $\mathbf{u}$ . The medial portion of the anterior lens curve is considered fixed, which means that the displacement vector does not deform. However, the

lateral anterior lens curve and the entire posterior lens curve are considered a free boundary, which means that they will deform. Next, the inelastic strain tensor is needed. The equation that is used is,

$$\varepsilon_{inel} = \varepsilon_{th} \quad (\text{Eq 3.20})$$

The inelastic strain tensor is equal to the thermal expansion strain tensor because the simulation is only concerned with the thermal expansion. To solve the thermal expansion strain tensor, the Thermal Expansion module is used. This gives the equation,

$$\varepsilon_{th} = \alpha * (T - T_{ref}) \quad (\text{Eq 3.21})$$

In this equation, the thermal expansion coefficient is defined by  $\alpha$ . Given that the deformation, inelastic, and thermal strain tensors are known, the elastic strain tensor can be calculated using the simple formula,

$$\varepsilon_{el} = \varepsilon - \varepsilon_{inel} \quad (\text{Eq 3.22})$$

The final portion of finding the stress tensor defines the stiffness matrix, or **C** in Equation 3.16. Because prior research has given uniform values for the lens, the solid model is assumed to be isotropic. Also, prior research has given the Young's Modulus and Poisson's ratio. Given the values, COMSOL only needs those two variables specified to calculate the stiffness matrix.

#### 3.2.4 Overview of the Independent Variables

The goal is to find the ideal collimation design, power setting, and pulse width to safely operate on the eye for the simulation.

To test for the collimation design, the affected variable is the laser radius. For the first collimation design, the radius of the laser is 287 micrometers. However, the second collimation design has a laser radius of three-fourths of a micrometer. Using the assumption that the laser beam area is circular, the mathematical formula for a circular area can be used to find the beam

area for both collimations. This then shows that the area for the first beam collimation is over one hundred thousand times larger than the second collimation. Seeing that the equation of irradiance for the laser is (Mirnezami, Jafarabadi, & Abrishami, Temperature Distribution Simulation of the Human Eye Exposed to Laser Radiation, 2013),

$$E = \frac{\text{Laser Power}}{\text{Beam Area}} \quad (\text{Eq. 3.23}),$$

the second collimation will have an easier time reaching a higher irradiance or more efficient at reaching a lower irradiance than the first collimation due to the vastly smaller area. However, this higher irradiance does come at the cost of having a much smaller range of safe operating power ranges.

Next, power setting is key to heating the lens. If the power is too high, the lens will heat up quickly past the ideal temperature and pressure. This event will cause surgical and health issues that will be detailed in the next section. However, if the power is too low, the eye will either not reach the ideal temperature range or will not reach the temperature range at an ideal time. A range of ideal power settings must be achieved to find and prepare for any further trials on living subjects.

Finally, the pulse width, or the length of time that the laser is at an active state, will act as the vehicle to induce the cavitation mechanism. When the laser is on, the lens of the eye will heat up exponentially. The rapid increase in thermal energy will then, in turn, result in a quick rise of pressure into the eye, which is the cavitation mechanism. Here, the pulse width is used to adjust the amount of time that the thermal energy can transfer into the cataract lens. There is currently no data on how a laser, like the proposed device, will function in the ocular lens. This due to a slightly larger wavelength compared to commercial femtosecond laser and vastly larger pulse

width. Since the device will work differently from the commonly used femtosecond laser, the available data can only show a trend of what to expect from the new laser device.

However, there is a secondary issue that the pulse width could attribute. There is a more significant chance that the patient will undergo severe damage to ocular structures from thermal damage with a higher pulse width. As pulse width is longer, there will have to be a larger fluence present to create the cavitation phenomena. This could lead to tissue damage that will be covered in the following section.

### 3.2.5 Targets of the Dependent Variables

For this simulation, the operation must accomplish two conditions. First, the pressure of the eye must be at least under two bar above atmospheric conditions. Second, the operation requires that there is no damage to ocular structures besides the cataract lens.

With the pressure of the cataract lens, the current cataract surgical operation and the prototype operation discussed in this thesis require cavitation, or the fast generation of pressure that results in the creation and collapse of bubbles in liquids. Now, the goal of both operations is to create the cavitation phenomena in the liquid zone of the lens near the cataract at the center of the eye. To do so, the nucleus and surrounding region of the cataract must be under 2 bar over atmospheric pressure to ensure cavitation (Zacharias, 2008). As seen in the paper “Role of cavitation in the phacoemulsification process,” the presence of cavitation was reduced as the pressure rose, with cavitation wholly gone once the environment reached above 2 bar above atmospheric conditions. Now, in the paper detailed, the pressure-reduced cavitation was occurring with the ultrasound phacoemulsification process rather than the femtosecond process. However, this will still be considered a goal due to that the proposed device requires cavitation rather than a “jack-hammer” effect that the ultrasound process requires.

Avoiding damage to other biological tissues is a significant consideration in creating a novel surgical technique. For this simulation, finding the ideal conditions ensures phacoemulsification and minimizes or eliminates any damage to surrounding structures from the temperature increases. Since the aqueous humor will achieve natural convection due to the heating of the lens, the heat transfer to the cornea could create a possibility of damaging the corneal tissue either temporarily or permanently. As for the damage to the iris, with most phacoemulsification processes, the iris is pulled back from the lens to ensure enough space for the probe to enter, thus why the iris has minimal contact with the lens in the model, as previously shown.

### **3.3 Results**

#### **3.3.1 Effects of Power**

Seeing that, in Equation 3.22, the power affects the irradiance of the laser, a trend of a higher maximum temperature within the eye will be seen with increasing laser power. However, this section looks at what the highest reached temperature will be at the refractive center of the eye. As expected, the increasing power did increase the maximum temperature in the lens capsule. Table 3.4 shows a clearer picture of the relationship between the power and maximum reached temperature.

Table 3.5: Approximate Maximum Temperatures at the Refractive Center of the Human Lens under a Continuous Pulse Width and Laser Radius of 287  $\mu\text{m}$

Power (mW)	Max Temperature ( $^{\circ}\text{C}$ )
0	36.8
500	150
1000	260
1500	375
2000	475
2500	600
3000	725

It is also important to note that there was no damage on the corneal tissue in the cases of 500 milliwatt and no applied power. In the other cases, complete damage to corneal tissue occurred. Further, the stress pressure curves were identical in shape, which shows a direct correlation to temperature. This relationship is shown in Figure 3.1 and Figure 3.2.

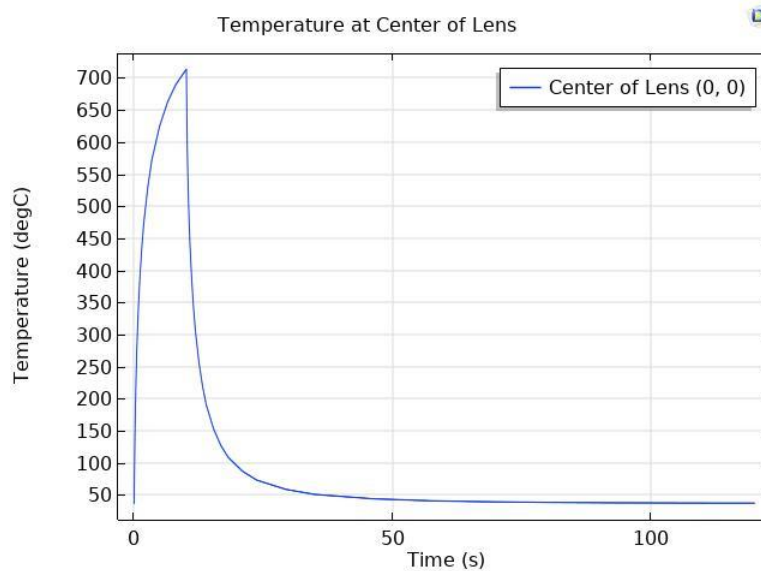


Figure 3.2: Temperature of the Refractive Center of the Eye at Laser Radius 287  $\mu\text{m}$  and Laser Power 3000 Milliwatt with No Pulse

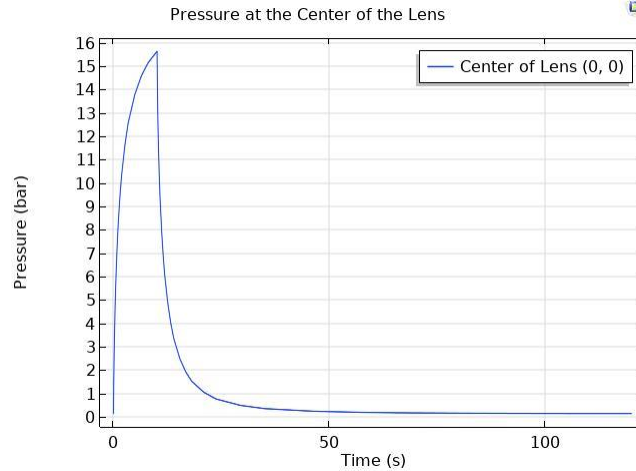


Figure 3.3: Stress Pressure of the Refractive Center of the Eye at Laser Radius 287  $\mu\text{m}$  and Laser Power 3000 Milliwatt with No Pulse

Unfortunately, in all cases, the stress pressure exceeded the two-bar threshold that was previously stated. When accounting for the massive damage dealt with corneal tissue and excessive pressure in the lens, an applied laser pulse could prove helpful.

Additionally, the continuous mode led to immediate damage to the cornea. This is highlighted in Figures 3.4 and 3.5. Because the temperature at all points along the cornea center exceeds sixty-five degrees Celsius, the center of cornea will undergo necrosis, which will cause a complete failure in the surgery.

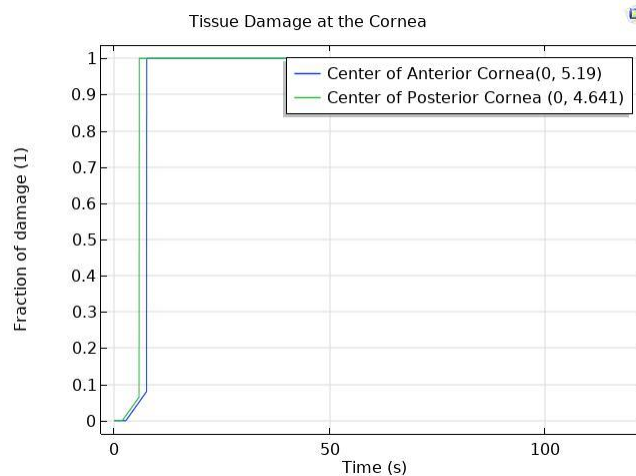


Figure 3.4: Tissue Damage at the Center of the Anterior and Posterior Cornea at Laser Radius 287  $\mu\text{m}$  and Laser Power 3000 Milliwatt with No Pulse

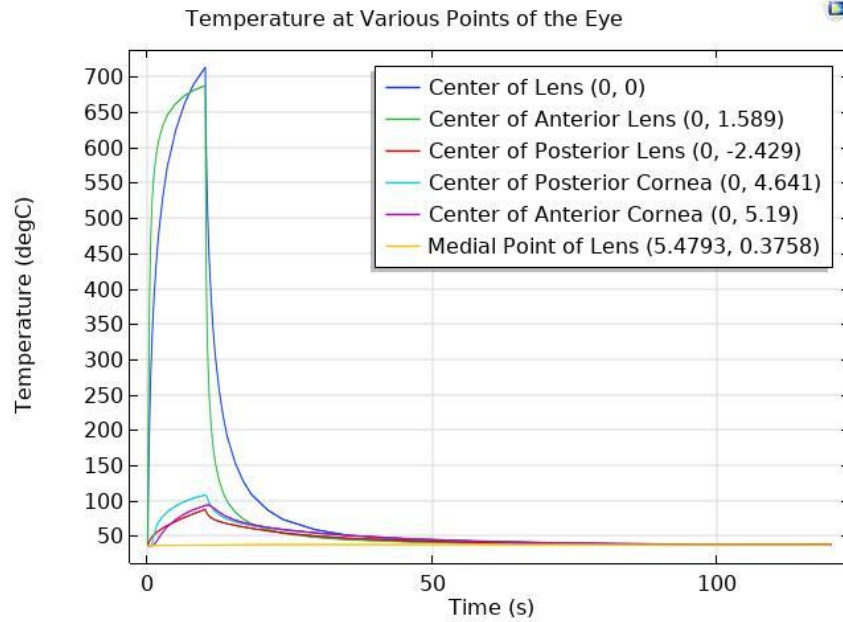


Figure 3.5: Temperature at Various Points of the Eye at Laser Radius 287  $\mu\text{m}$  and Laser Power 3000 Milliwatt with No Pulse

### 3.3.2 Effects of Pulse Width

Interestingly, pulsing the laser greatly affected the maximum temperature of the refractive center of the lens. By adding a pulse width, the maximum temperature that occurs in the refractive center of the lens is significantly reduced. This is due to the time that the laser is not in operation between pulses. During the pauses in between pulses, the biological material has a moment to cool rapidly. The phenomena are highlighted in Figures 3.6 and 3.7. The maximum temperatures of the refractive center of the lens at an array of different pulse widths are presented in Table 3.6. Here, the length of the pauses is equal to the respective pulse width.

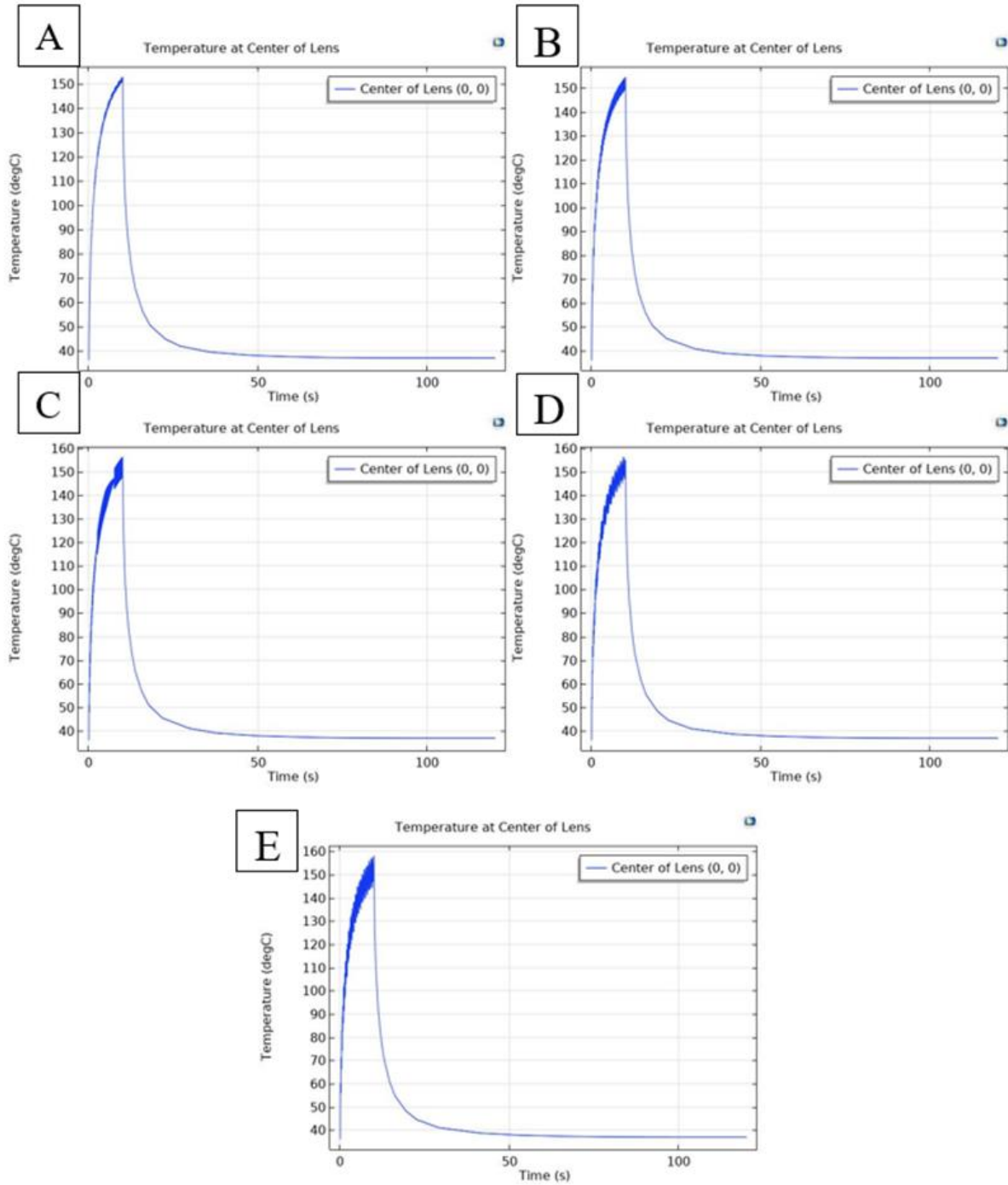


Figure 3.6: Temperature of the Refractive Center of the Eye at Laser Radius  $287 \mu\text{m}$  and Laser Power 1000 Milliwatt with (A) 10 Millisecond, (B) 30 Millisecond, (C) 50 Millisecond, (D) 70 Millisecond, and (E) 90 Millisecond pulse width (50% duty cycle)

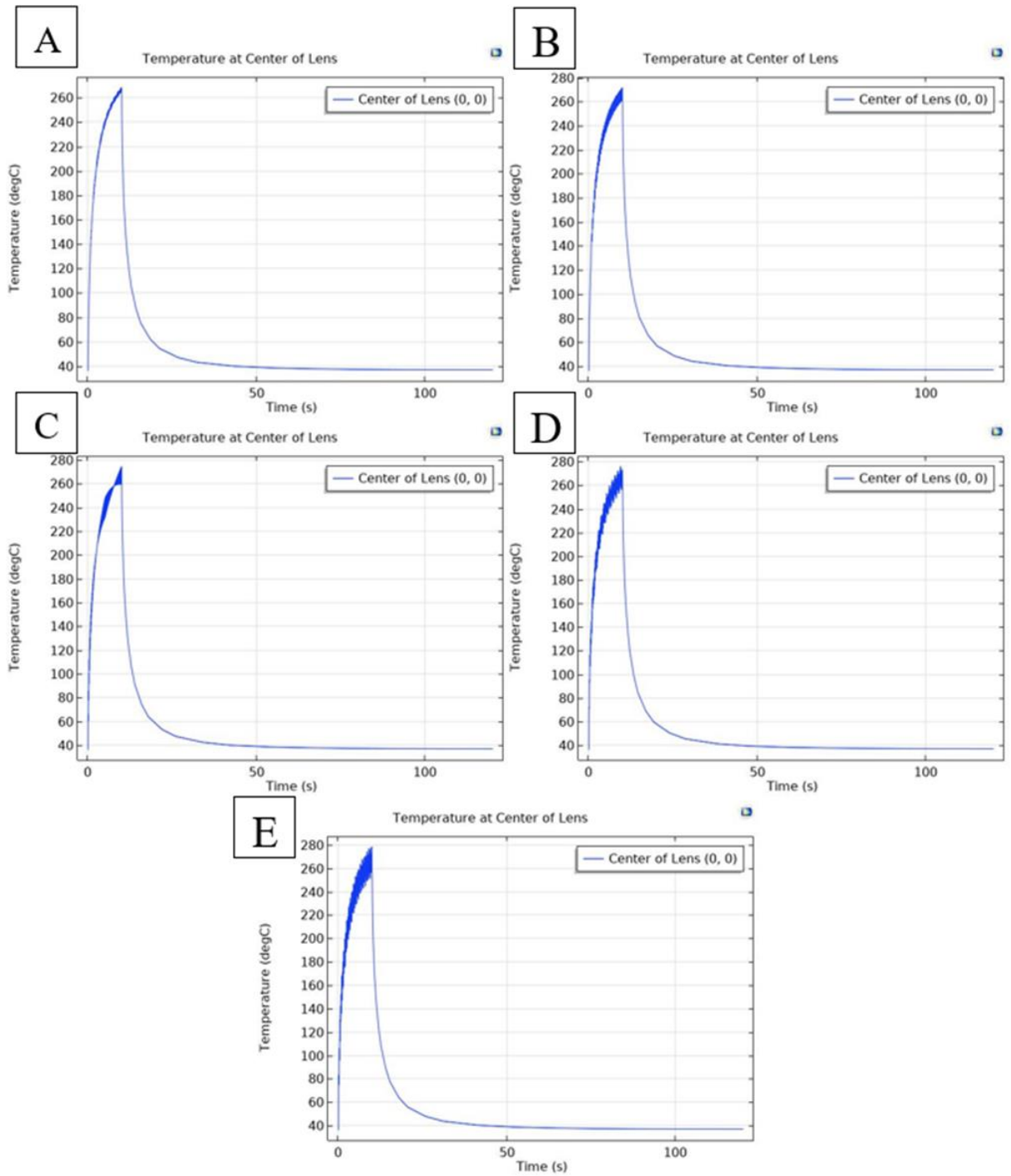


Figure 3.7: Temperature of the Refractive Center of the Eye at Laser Radius  $287 \mu\text{m}$  and Laser Power 2000 Milliwatt with (A) 10 Millisecond, (B) 30 Millisecond, (C) 50 Millisecond, (D) 70 Millisecond, and (E) 90 Millisecond Pulse Width (50% Duty Cycle)

Table 3.6: Approximate Maximum Temperatures at the Refractive Center of the Human Lens under Various Pulse Widths and Laser Radius of 287  $\mu\text{m}$

Power (mW)	Continuous	Max Temperature ( $^{\circ}\text{C}$ ) at				
		10 ms	30 ms	50 ms	70 ms	90 ms
500	150	95	95	97	98	97
1000	260	155	160	155	155	155
1500	375	210	215	215	215	215
2000	475	270	270	275	275	280
2500	600	325	330	335	335	340
3000	725	380	385	390	395	400

The considerable reduction of the temperatures is exciting, but that is one portion of the overall parameter selection. The tissue damage is a significant factor in selecting the power and pulse widths that will be selected for testing. Unsurprisingly, the lower temperatures did lead to a broader array of options to select for testing. However, in one case, the power setting of 2000 milliwatts was eligible for selection at 50 milliseconds. This was not expected but was found to be quite interesting.

Table 3.7: Tissue Damage at the Refractive Center of the Human Lens under Various Pulse Widths and Laser Radius of 287  $\mu\text{m}$

Power (mW)	Continuous	Tissue Damage at				
		10 ms	30 ms	50 ms	70 ms	90 ms
500	NO	NO	NO	NO	NO	NO
1000	YES	NO	NO	NO	NO	NO
1500	YES	NO	NO	NO	NO	NO
2000	YES	YES	YES	NO	YES	YES
2500	YES	YES	YES	YES	YES	YES
3000	YES	YES	YES	YES	YES	YES

Given the wide selection of choices, the millisecond phacolytic laser should hopefully find a suitable lasing condition to emulsify the toughest cataracts and avoid harm to the patients.

### 3.3.3 Effects on Collimation

Seeing that the laser radius that was performing the previous experiments was slightly large, the possibility of a smaller laser probe being built is present. The second collimation design has a radius of three-fourths of a micrometer. When taking Equation 3.22 into account, the laser intensity does change based on the beam area. As expected, by reducing the area, the maximum temperatures are higher than in the first collimation design. However, this is easily remedied by reducing the laser power by a factor of one hundred. The pulse widths also provide a similar reduction in the cooling and heating patterns seen in the previous section. Table 3.8 shows a brief example of how adjusting the second collimation's power can show similar results from the first collimation from the previous two sections.

Table 3.8: Maximum Temperature at the Refractive Center of the Human Lens under Various Pulse Widths and Laser Radius of 287  $\mu\text{m}$

Power (mW)	Maximum Temperature ( $^{\circ}\text{C}$ ) at	
	Continuous	10 ms
500	1750	1500
50	975	380
5	100	70

As seen from the experimental results above, slight adjustments to lower the power will alleviate the higher temperatures that the smaller area will bring with it.

### 3.4 Conclusion

Given the observed results, the available options to test the milliwatt laser are numerous. This provides plenty of ways to exceed the ablation threshold barrier that currently poses as the

main challenge. However, there are a few conditions that were neglected that could harm or help the chances of further success. As some may notice, the presence of the probe itself was largely ignored. The presence of the probe could become an issue by providing a secondary heat source that could harm the patient. However, it can also provide a heat sink system that could further avoid corneal tissue damage by absorbing the energy that is provided by the laser. Further testing will be necessary to observe how the laser will operate in a real-world scenario.

Also, the changes in the probe radius showed that thermal damages could be simply avoided by lowering the temperature by about a factor of 100. This shows that replacing or changing some aspects of the probe should be simple if an action like that must be taken.

## **Chapter 4: Construction of the Phacolysis Device**

### **4.1 Considerations for the Device**

Before beginning the design and construction process of the phacolysis device, the purpose for why this device is being built must be recalled. This device's primary purpose is to treat rural communities in developing countries. Because of this, the device must be cheap to produce and must be portable. With these characteristics, the surgeries will be cheaper due to the much lower cost of the equipment. Another design element that needs to be incorporated is ensuring that the device is thermally stable due to the heat generated by the laser diode.

Realizing these necessities, the device must be able to be carried in a standard backpack. The device must be light enough to allow the physician to easily transport the device within a backpack without injuring their back and shoulders during longer distances. Also, the terrain could get rough on the journey to patients, so the device must be durable enough to sustain some significant impacts. Given this, the laser mount, or the container and any internal components, would be one of the most critical components of the phacolysis device.

### **4.2 Laser Mount**

#### **4.2.1 Discussion of the Needs of a Custom Design**

Initially, the LDM90/M laser mount model by Thor Labs was deemed reasonable to be the housing for the phacolysis device. Unfortunately, the mount could not handle the required specifications needed to support the operation and was rendered unusable after a short test run. Upon further analysis, the LDM90/M had some major flaws when used for the phacolysis device.

First, the LDM90/M had a maximum current input of two amps. As seen in Chapter 3, the laser diode is expected to reach power levels of anywhere from 500 milliwatts to 2500 milliwatts, which would require up to seven amps. Seeing that the circuit design has to be redesigned, the accompanying mount must house the changed circuit properly. Second, the LDM90/M mount had a maximum laser current of two amps. Though at the time this seemed reasonable, the laser diodes that would be capable of pulsing and reaching high voltages around three volts required around eight amps. This was the primary reason that the LDM90/M's circuit was burnt after the short test. Lastly, the LDM90/M was not able to suitably dissipate heat from the laser diode. If the circuit could operate with the necessary power and amperage, the circuit and laser damage would have been damaged from the high temperatures within the mount and on the surface due to the limited surface area.

Given the extent of these issues, a custom design for a laser mount was needed—the creation of the custom laser mount needed to be divided into sections. First, the outer shell of the laser mount would need to have enough surface area to cool the heat generated from the diode efficiently. Second, the circuit needs to sustain the voltage and amperage that the diode and other internal components require. Finally, the selection and, possibly, creation of the internal components needs to be considered.

#### 4.2.2 Design of the Circuit

The circuitry of the mount is the most integral part of the custom-made mount. Without it, the mount will not be able to cool or deliver current to the diode properly. To reduce the complexity of repairs, the circuit design was split into two different circuit boards. This helps remove a damaged circuit from the mount to repair quickly or replace at a rapid pace. The diagrams of the circuit boards are seen in Figures 4.2 and 4.3.

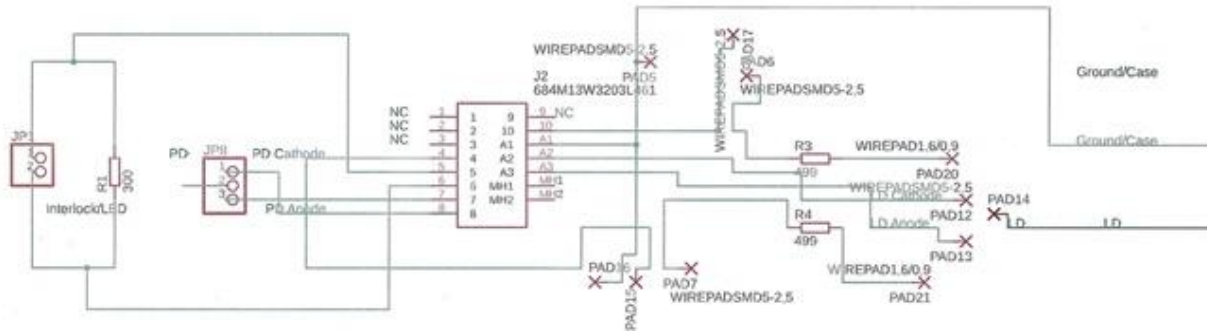


Figure 4.1: Circuit Diagram of the Laser Diode Board

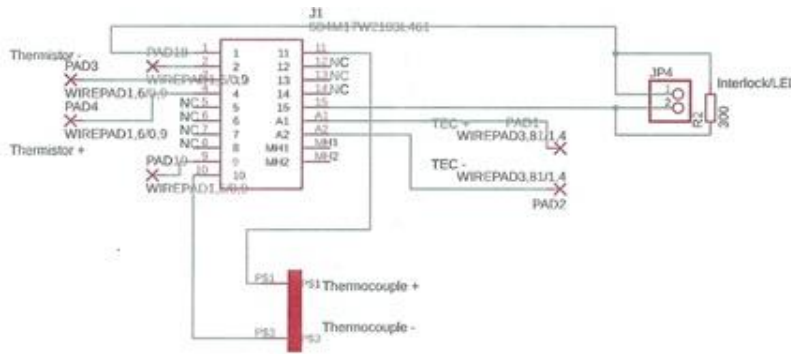


Figure 4.2: Circuit Diagram of the Thermal Components Board

As Figure 4.2 shows, the laser diode circuit board only comprises the laser diode. This is because the laser diode requires a specialized design to help compensate for the diode experiences' pulsing modes. The thermal components, however, have their separate board because their functions rely on each other. This board contains the connections to the thermistor and thermo-electric cooler, noted as TEC on the diagram. When combined, the thermistor detects the temperature of the inserted copper plate, and the TEC acts as a control system to keep the copper plate at a set temperature while using the thermistor data to detect how much the TEC needs to cool the plate.

#### 4.2.3 Design of the Outer Shell

When it comes to the cost of the laser mount, the outer shell is the most expensive component of the laser mount. This is primarily due to the materials, processing, and design of

the shell. The outer shell is the most complicated portion of the solid design, from holding significant components and some intricate internal designs. To thoroughly explain the various features and assumptions made, the creation of the outer shell will be broken down into various pieces.

To begin, the outer shell is the central containment for the laser diode. As one may expect, the laser diode is the primary source of heat within the laser mount. To account for this, the material must withstand a significant heat source since the exact heat load is not yet defined. Also, as previously stated, the mount must endure multiple hazards that remote areas may contain. For this prototype, aluminum was chosen due to its high thermal diffusivity and notable strength. This material also helps that it is cheap to use in production, which helps further to ensure affordability.

Next, the outer shell holds the circuit and other vital components. As discussed in the previous section, the circuit board is 210 millimeters, or approximately eight and a quarter inches, long and 80 millimeters, or about 3 inches, wide. To account for this, the interior chamber of the shell is 216 millimeters long and 144 millimeters wide. The extra space is created to ensure that the electrical currents and heat from the circuit and mount do not interfere.

However, the interior chamber does require two parts that are integral for the cooling process to prevent the laser diode from thermal damage. These two parts are cooling columns that are placed on the ceiling of the back plate. The column centers are 35 millimeters from the center of the interior chamber along the width and level along the length. The base of the columns has a length and width of 40 millimeters. Now, the cooling columns are to connect with the thermoelectric coolers (TECs) that are attached to a copper plate, which both parts will be discussed in a later section. Based on the TECs and copper plate dimensions, the columns have a

height of 47.45 millimeters to ensure that they touch both the TECs and the ceiling of the backplate.

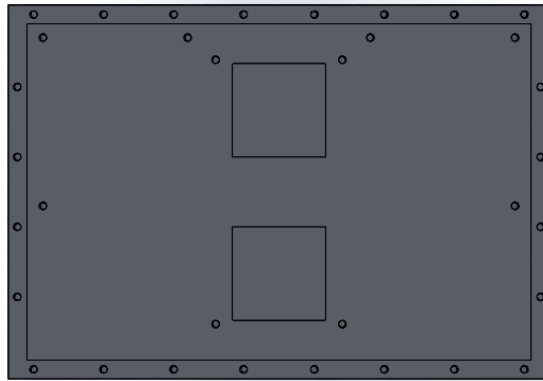


Figure 4.3: Interior View from the Bottom View

Further, as detailed further in the next section, the mount faced extensive thermal heating, even with the addition of the cooling columns and the TECs. To address this issue, thermal fins and four small fans were added. The following section details the addition of the thermal fins in greater detail, but the addition of the fans is discussed here. The WINSINN 50mm High-Speed fans were chosen to add a convective means of heat transfer. To properly attach the fans, two large holes, with a diameter of 50 millimeters, were added on each side. Each hole was even at the center of the height of the outer shell and 42.5 millimeters from the center along the width. The fans were placed in a way where one side of the length would transport air from the environment into the mount, with the other side sucking the air inside of the mount out of the mount. This is because the constant flow of air from the environment into the mount and then back out should keep the interior chamber of the mount around the environment's temperature.

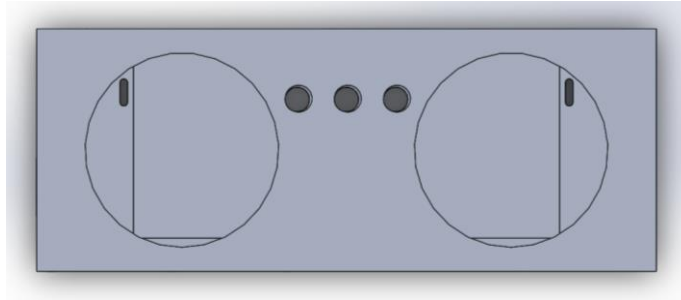


Figure 4.4: Side View of Fan and Mount Screw Placements

Finally, as seen in Figure 4.3, there are three holes in between the fans. These are used to mount the phacolysis device to another surface or elevation platform. The mounting holes are at the exact specifications of the LDM90 ThorLabs laser mount.

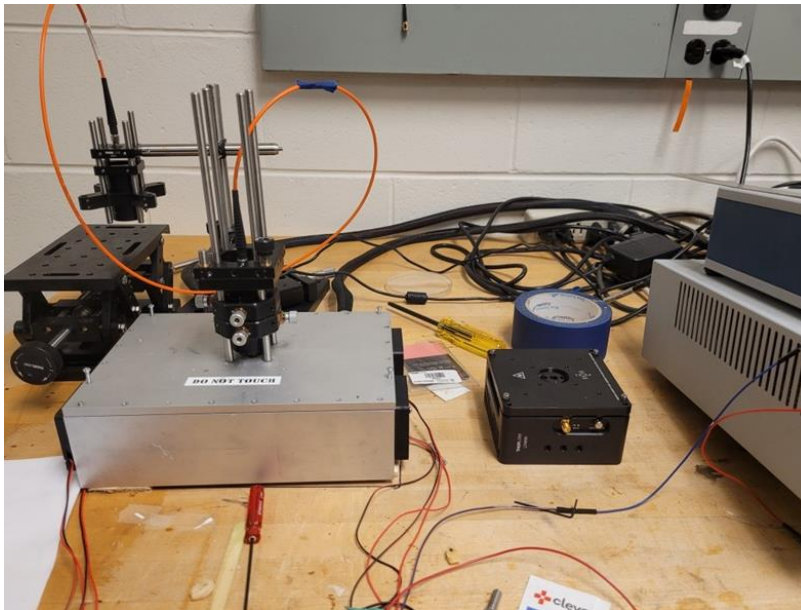


Figure 4.5: Prototype Custom Mount (Left) and LDM90/M (Right) Pictured Side by Side

#### 4.2.4 Discussion and Theory on the Addition of Thermal Fins

To relieve the heat generated by the phacolysis laser, both fans and thermal fins were added to the device's back plate. Here, the thermal fins were added to the three sides of the cooling columns that are not facing each other. The addition of thermal fins helps the cooling columns add more surface area to increase conduction-based cooling, which helps disperse the

heat across a more considerable amount of space. However, when adding thermal fins, it is essential to analyze the overall performance of the fins to ensure that proper cooling can take place.

To begin the analysis of the fins, various properties must be defined. These properties are the thermal conductivity, thermal diffusivity, and the dimensions of the fin. For the analysis in this paper, the Awxlumv Heat Sink 40 x 40 x 11mm Aluminum Small Heatsink is used going forward. The properties of the heat sink are defined in Table 4.1.

Table 4.1: Properties of Analyzed Thermal Fins

Thermal Conductivity (W/m/K)	201
Thermal Diffusivity (W/m <sup>2</sup> /K)	35
Total Length (mm)	40
Total Height (mm)	11
Base Height (mm)	2
Fin Height (mm)	9
Fin Width (mm)	1.1
Number of Fins	13
Distance Between Fins (mm)	3.241

The first step of the analysis of the thermal fins is to find the heat energy loss of a single fin. To accomplish this, the formula below is used (Incropera & Dewitt, 2011),

$$q_f = \sqrt{h * P * k * A_c} * \theta_b * \frac{\sinh(m * H_f) + \left(\frac{h}{mk}\right) \cosh(m * H_f)}{\cosh(m * H_f) + \left(\frac{h}{mk}\right) \sinh(m * H_f)} \quad (\text{Eq. 4.1})$$

In this equation, thermal diffusivity in units of Watts per squared meter per Kelvin is denoted as h, thermal conductivity in units of Watts per meter per Kelvin is shown as k, and the height of the fin in units of meters is represented as H<sub>f</sub>. The symbol  $\theta_b$  is used to show the difference between the temperature, in Kelvin, of the base and the surrounding environment. Now, there are

some new symbols used. These are the perimeter, or  $P$ , and the area, or  $A_c$ , of the cross-sectional area of the contact area between the fin and base (Incropera & Dewitt, 2011). Further, the constant  $m$  is a constant, in units of inversed squared meters, used for the simplicity of deriving the equation. Here,  $m$  is equal to (Incropera & Dewitt, 2011),

$$m^2 = \frac{h * P}{k * A_c} \quad (\text{Eq. 4.2})$$

Given the equations above, Table 4.2 shows the resulting values found for the heat energy loss in a single fin.

Table 4.2: Heat Loss from Single Fin

Contact Area (mm <sup>2</sup> )	44
Contact Perimeter (mm)	82.2
Base Temperature (°C)	75
Environment Temperature (°C)	25
$\Theta_b$ (°C)	50
$m$ (1/mm)	18.04
Heat Loss from Single Fin (W)	8.80

The final step to ensure that the thermal fins are adequate is to find the total heat loss from the addition of the thermal fins. To find this, the total heat loss equation is shown as (Incropera & Dewitt, 2011),

$$q_t = h * A_t \left( 1 - \frac{N * A_f}{A_t} * (1 - \eta_f) \right) * \theta_b \quad (\text{Eq. 4.3})$$

This equation uses some new symbols that have not been explained. First,  $N$  is simply the number of fins present on the applied fin product. Next,  $A_t$  is the representation of the surface area of the surface that contains the fins and the entire surface area of the fins. Finally,  $\eta_f$  is the unitless efficiency of the heat loss of a single fin. The efficiency is calculated as (Incropera & Dewitt, 2011),

$$\eta_f = \frac{q_f}{h \cdot A_f \cdot \theta_b} \quad (\text{Eq. 4.4})$$

Given the equations above, the total heat loss from the applied fin device can be seen in Table 4.3.

Table 4.3: Total Heat Loss from Fin Device

Total Area (mm <sup>2</sup> )	4154
Efficiency of Single Fin	0.99
Total Heat Loss (W)	45.98

Seeing the high loss and aluminum's low heat capacity, the fin device was deemed an acceptable purchase to add to the phacolysis device. However, the fins came with double-sided adhesive tape that, upon further inspection, had horrible thermal properties that did not help the fins act as calculated.

### 4.3 Laser Diode

The laser diode is the main component that ensures that the phacolysis device performs its designed functions. Due to requiring a high voltage, finding the correct diode proved to be a challenge. However, the ThorLabs L1480G1 (specification,  $\lambda=1480$  nm,  $p=3$  W) laser diode was the best available diode on the market to accomplish the needed specifications. This laser diode has a maximum power output of 3.2 watts, which is higher than the simulated laser output powers tested. The laser also has a typical laser wavelength of 1480 nanometers, which keeps the laser output within the infrared wavelength range. However, this diode does require a large operation current of at least three amps. This does pose an issue for later if a controller is needed to be created more compactly.

This specific diode was chosen due to water's absorption coefficient at 1480 nanometers. The liquid within the lens was assumed to be like water, although some substances were

dispersed within. Based on this information, the absorption coefficients across the spectrum of near-infrared light of water showed a noticeable peak at around 1480 nanometers (Ruru, Yingqing, Yan, Qidong, & Lei, 2012). However, when looking at a spectrum of absorption coefficients in the lens media, this behavior is mirrored as expected. The lens media was found to have a similar peak and behavior to that of water at 1480 nanometers (van den Berg & Spekreijse, 249-253).

## **Chapter 5: Experimentation on Gelatin**

### **5.1 Introduction**

The key obstacle to the fundamental research is if utilizing millisecond pulses leads to a cavitation phenomenon that could lead to the emulsification of the cataract. To test the laser's pulsing capabilities, gelatin samples were made to be similar in opacity to a cataract. These experiments aimed to see if the pulsing on the laser reduces the dispersion of heat and if a cavitation event occurs. A clearer picture of how the surgical process will occur in the lens is created by studying these parameters.

### **5.2 Methods and Materials**

#### **5.2.1 Creation and Analysis of the Gelatin Samples**

For properly experimenting with developing cataract laser surgery, a set of sample cataracts is needed for replicable experimentation. To do this, phantom gel cataract samples were determined to be one solution for the pilot experiments. A series of cataract samples were created with different concentrations and surveyed among optometrists.

##### *5.2.1.1 Phantom Gel Cataract Sample Creation*

The cataract samples were created similarly as described in the paper by Farrer, Odéen, et al. Prior to creating the cataract samples, various concentrations, listed in Table 5.1, were accepted for this round surveying. These concentrations were considered based on the paper named above, intermediates between the paper's values, a maximum value of the gelatin's solubility in heated water, and a minimum value to give both clarity and some structural strength.

Table 5.1: Accepted Concentrations from the Survey Performed

Formulation Label	Mass of Gelatin per 750 mL of Water (g)	Mass of Gelatin per 1 mL of Water (g)	Mass of Gelatin per 50 mL of Water (g)
A	25.00	0.03	1.67
B	50.00	0.07	3.33
C	111.00	0.15	7.40
D	166.50	0.22	11.10
E	222.00	0.30	14.80
F	277.50	0.37	18.50
G	333.00	0.44	22.20

For the creation of the cataract samples, gelatin from porcine skin, with a gel strength of 90-110 g Bloom, from Sigma-Aldrich (Product Number G6144, Type A) and tap water were used. To begin the process, 50 milliliters of water were placed in a 150 mL beaker, the desired amount of gelatin powder was measured on balance, and the heat plate was raised to about 200 degrees Celsius. While the heat plate is heating up, the beaker of water was placed on the heat plate to start the heating process. When the water started to boil, the gelatin powder was added incrementally and stirred to ensure that the powder could disperse in the water and avoid clumping of the gelatin. Once the entire gelatin powder has been placed in the solution, the solution was poured into a series of petri dishes where the height of the solution was around 5 millimeters. The solution's height restriction matches the approximate average height dimensions seen in lenses across all cataract gradings (Henriquez, Mejias, Rincon, Izquierdo Jr., & Binder, 2019). After pouring, the samples were immediately placed in a refrigerated setting for about 24 hours. Finally, pictures of the samples were taken once solidified for placement on the survey, shown in Figure 5.1.

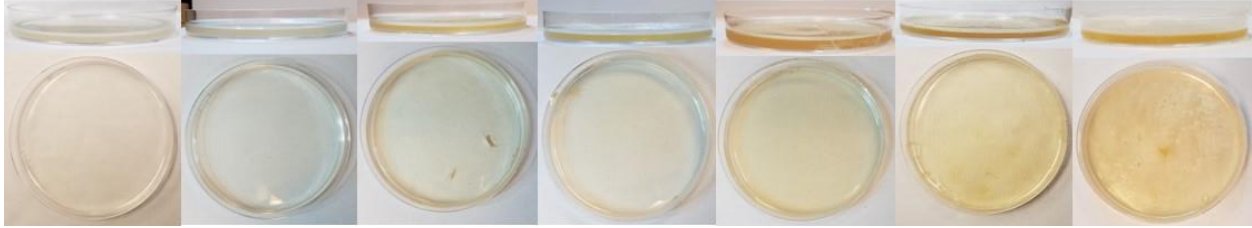


Figure 5.1: Photograph Scale of the Formulations Used for Gelatin Experiments

#### 5.2.1.2 Survey for Grading

To gather data on the grading of the cataract samples, a survey was distributed to six ophthalmologists. The survey consisted of eight questions: seven questions consisting of the grading of one of the cataract samples and one question on any improvements to the surveying method. The ophthalmologists were asked to grade for nuclear opacity and nuclear color with the seven grading questions, both on a 0 to 5 scale, based on the Lens Opacities Classification System III (LOCS III). These details were asked because the cataract samples mimic the common nuclear cataracts seen in many patients. The seven grading questions were also placed randomly to avoid any possible bias from seeing the prior samples. The survey was distributed via Google Forms.

#### 5.2.1.3 Results of Grading

As seen in Figure 5.2, the optometrist grading system shows subjective variability. Interestingly, the mean line shown in the figure shows a sigmoidal curve that flattens out around grade 4. However, as concentration exceeded 50 mg of gelatin per 750 mL of water, outliers became increasingly present. For example, the mean grade of the 222 mg of gelatin per 750 mL of water is about 3, but an outlier grade of 1 is present in the same set.

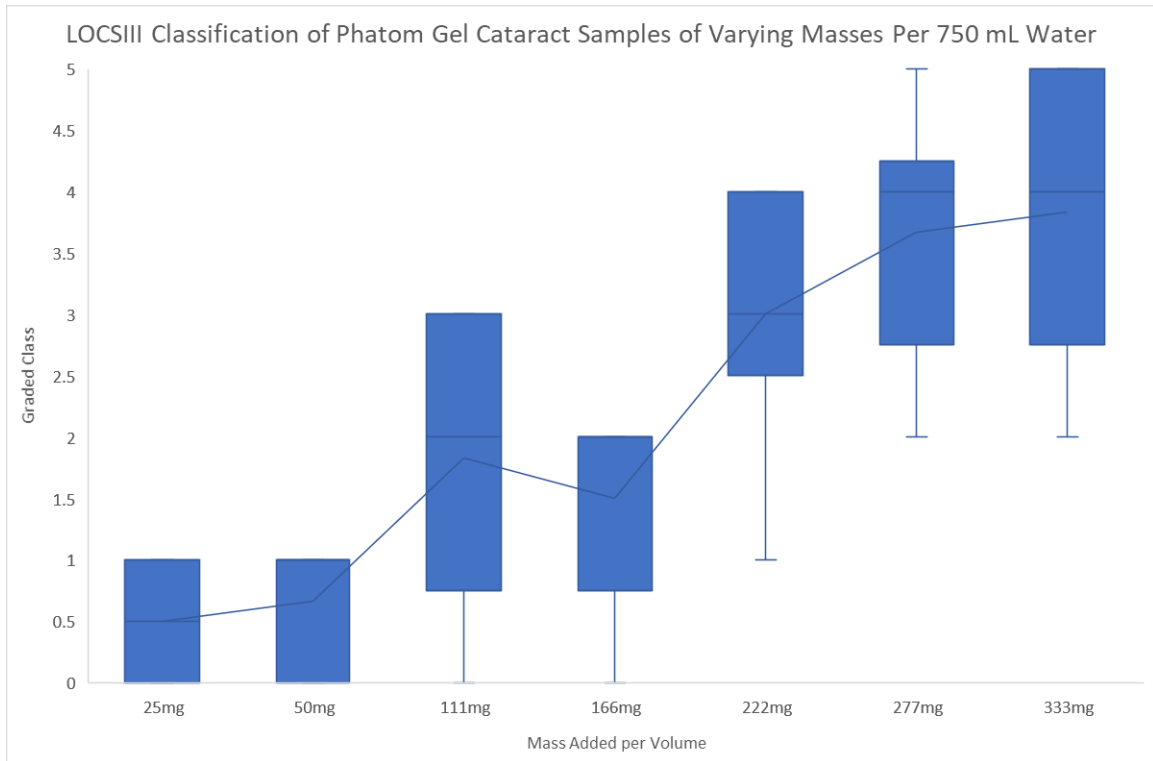


Figure 5.2: LOCS III Classification of Phatom Gel Cataract Samples of Varying Masses Per 750 mL of Water

The means, standard deviations, maximum values, and minimum values are detailed in Table 5.2. As seen in this table, the grading begins to have a higher standard deviation as the color starts to become noticeable. When it comes to the dip seen in the 166 g of gelatin per 750 mL of water, the possible background coloring is seen in some of the sample pictures or lighting occurring from above could have contributed to the lower score as well as that the sample could be simply more apparent to the observer.

Table 5.2: Statistical Values by the Cataract Sample Survey

Formulation Label	Mass of Gelatin per 750 mL of Water (g)	Mean	Standard Deviation	Minimum Value	Maximum Value
A	25.00	0.50	0.55	0	1
B	50.00	0.67	0.52	0	1
C	111.00	1.83	1.17	0	3
D	166.50	1.50	0.84	0	2
E	222.00	3.00	1.10	1	4
F	277.50	3.67	1.03	2	5
G	333.00	3.83	1.17	2	5

### 5.2.2 Experimental Procedure

The laser diode system was used to perform phacolysis on the 7 gelatin phantoms. For this experiment, the laser power will be fixed at 1000 milliwatts while changing the pulse width. The pulse widths that will be used are the same that are used in the COMSOL simulation, which are 10, 30, 50, 70, and 90 milliseconds. Each pulse width will be tried on each formulation for a total of five trials. For the procedure, the laser will be aimed at one point of the gelatin and begin lasing. The laser will remain on until the gelatin liquefies or until five minutes are completed. The experiment will measure the time of liquification and the area of the liquid pool that is created. The measurement method will be based on an algorithm made on MATLAB to measure lengths of an area of interest within a photograph in pixels and convert them into length units. Further, the resulting data of each concentration will be tested to see if the resulting areas with pulse settings are statistically different from the area without a pulse by using the Wilcoxon

rank-sum test. The pulsed areas are considered statistically different from the continuous area if the calculated p-values are less than 0.05.

### **5.3 Results**

To break down the results, there will be two sections that describe the cataract samples that were graded less than 2.5 and samples that were graded more than 2.5. The following results tables will show the data for an individual concentration. This data is then divided by the data point's trial number with the corresponding pulse setting. The median area of thermal damage and the results (p-value) of the Wilcoxon rank-sum test comparing the areas of the pulsed laser trials to the continuous mode operation are shown.

#### **5.3.1 Graded Samples Less Than 2.5**

Interestingly, these samples began with a random distribution of thermal damage across all pulse settings with the lower concentration formulation and the higher concentration formulations making the slight but noticeable distinction of smaller areas of thermal damage. As seen in Figure 5.1, the data values of each subset of experimentation show a random placement of means on all pulse settings within the first formulation. This can be explained due to the high melting point of the gelatin mixture. Because the gelatin mixture could melt at room temperatures, the gelatin became a liquid in a wider area because the higher temperatures help initiate a faster melting process.

Table 5.3: Area (cm<sup>2</sup>) of Present Thermal Damage for Formulation A

	1	2	3	4	5	Median	p-Value
Continuous	0.426	0.312	0.388	0.339	0.261	0.339	-
10 ms	0.249	0.238	0.291	0.290	0.391	0.290	0.222
30 ms	0.369	0.389	0.369	0.372	0.360	0.369	0.5238
50 ms	0.338	0.293	0.314	0.213	0.224	0.293	0.1508
70 ms	0.254	0.285	0.278	0.346	0.330	0.285	0.3095
90 ms	0.348	0.403	0.473	0.335	0.333	0.348	0.5476

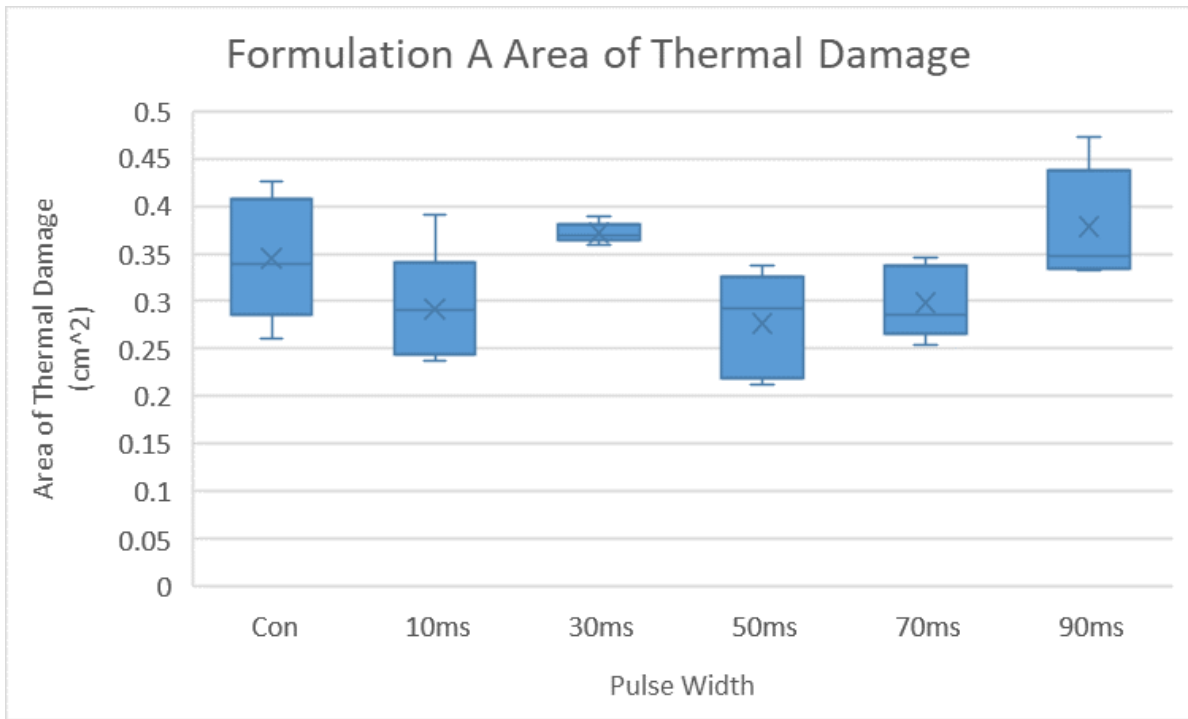


Figure 5.3: Area of Thermal Damage on the Surface of Formulation A Gelatins

With the higher concentrated formulations, the pattern of more contained areas of thermal damage becomes more apparent. However, the third formulation shows the exact opposite than expected. This could be explained through errors within the MATLAB algorithm or the photographs taken of the gelatin surface. It should also be added that the ninety-millisecond pulses on the fourth formulation did show a slightly higher than expected mean thermal area.

This could be showing that the ninety-millisecond pulses are not as effective at showing thermal containment as hoped.

Table 5.4: Area (cm<sup>2</sup>) of Present Thermal Damage for Formulation B

	1	2	3	4	5	Median	p-Value
Continuous	0.341	0.374	0.402	0.396	0.324	0.374	-
10 ms	0.155	0.287	0.217	0.222	0.247	0.222	0.008
30 ms	0.24	0.216	0.266	0.357	0.236	0.240	0.032
50 ms	0.229	0.169	0.171	0.272	0.472	0.229	0.151
70 ms	0.217	0.207	0.191	0.209	0.203	0.207	0.008
90 ms	0.283	0.225	0.308	0.228	0.285	0.283	0.008

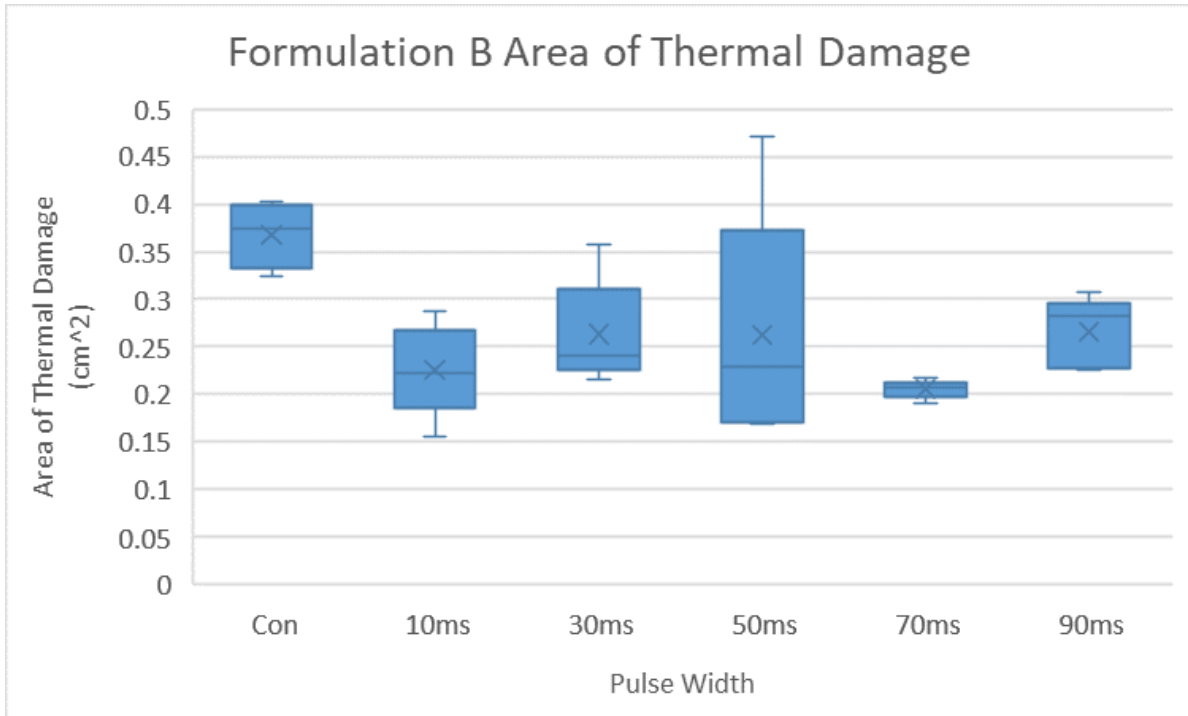


Figure 5.4: Area of Thermal Damage on the Surface of Formulation B Gelatins

Table 5.5: Area (cm<sup>2</sup>) of Present Thermal Damage for Formulation C

	1	2	3	4	5	Median	p-Value
Continuous	0.161	0.216	0.151	0.161	0.245	0.161	-
10 ms	0.105	0.157	0.227	0.198	0.126	0.157	0.397
30 ms	0.181	0.176	0.239	0.175	0.167	0.176	0.500
50 ms	0.205	0.14	0.144	0.146	0.213	0.146	0.191
70 ms	0.223	0.228	0.23	0.281	0.269	0.230	0.048
90 ms	0.247	0.305	0.307	0.363	0.3	0.305	0.008

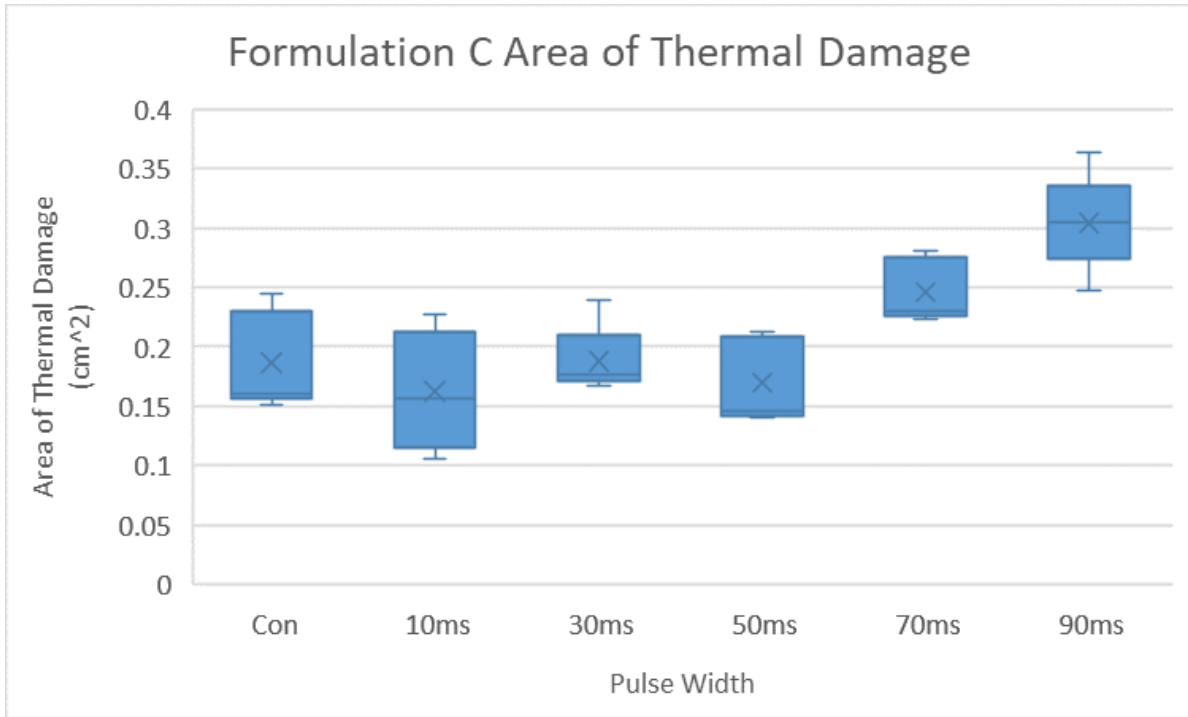


Figure 5.5: Area of Thermal Damage on the Surface of Formulation C Gelatins

Table 5.6: Area (cm<sup>2</sup>) of Present Thermal Damage for Formulation D

	1	2	3	4	5	Median	p-Value
Continuous	0.375	0.385	0.315	0.358	0.263	0.358	-
10 ms	0.2	0.197	0.168	0.164	0.116	0.168	0.008
30 ms	0.215	0.16	0.16	0.181	0.162	0.162	0.008
50 ms	0.143	0.151	0.143	0.154	0.129	0.143	0.008
70 ms	0.136	0.21	0.222	0.153	0.138	0.153	0.008
90 ms	0.235	0.288	0.266	0.375	0.221	0.266	0.167

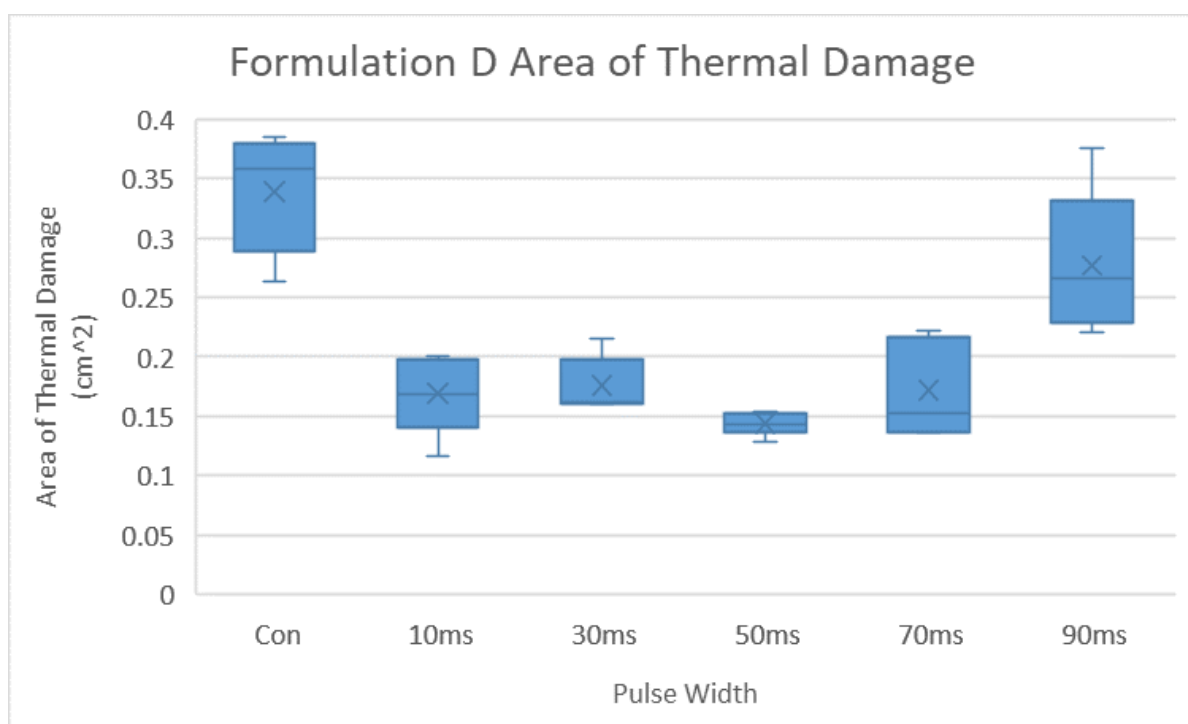


Figure 5.6: Area of Thermal Damage on the Surface of Formulation D Gelatins

### 5.3.2 Graded Samples More Than 2.5

The final three formulations showed a distinct difference in the areas of thermal damage when comparing the pulsed settings against the continuous settings. Although the sixth formulation did not show as strong of a pattern as the fifth and seventh formulation, the sixth

formulation did show a trend of smaller areas made with pulse settings than the areas created without a pulse setting, which is further highlighted by the p-value of less than 0.05.

Table 5.7: Area (cm<sup>2</sup>) of Present Thermal Damage for Formulation E

	1	2	3	4	5	Median	p-Value
Continuous	0.654	0.293	0.309	0.335	0.336	0.335	-
10 ms	0.051	0.037	0.047	0.054	0.063	0.051	0.008
30 ms	0.049	0.035	0.059	0.035	0.055	0.049	0.008
50 ms	0.049	0.057	0.04	0.035	0.035	0.040	0.008
70 ms	0.022	0.022	0.021	0.028	0.022	0.022	0.008
90 ms	0.029	0.04	0.037	0.037	0.032	0.037	0.008

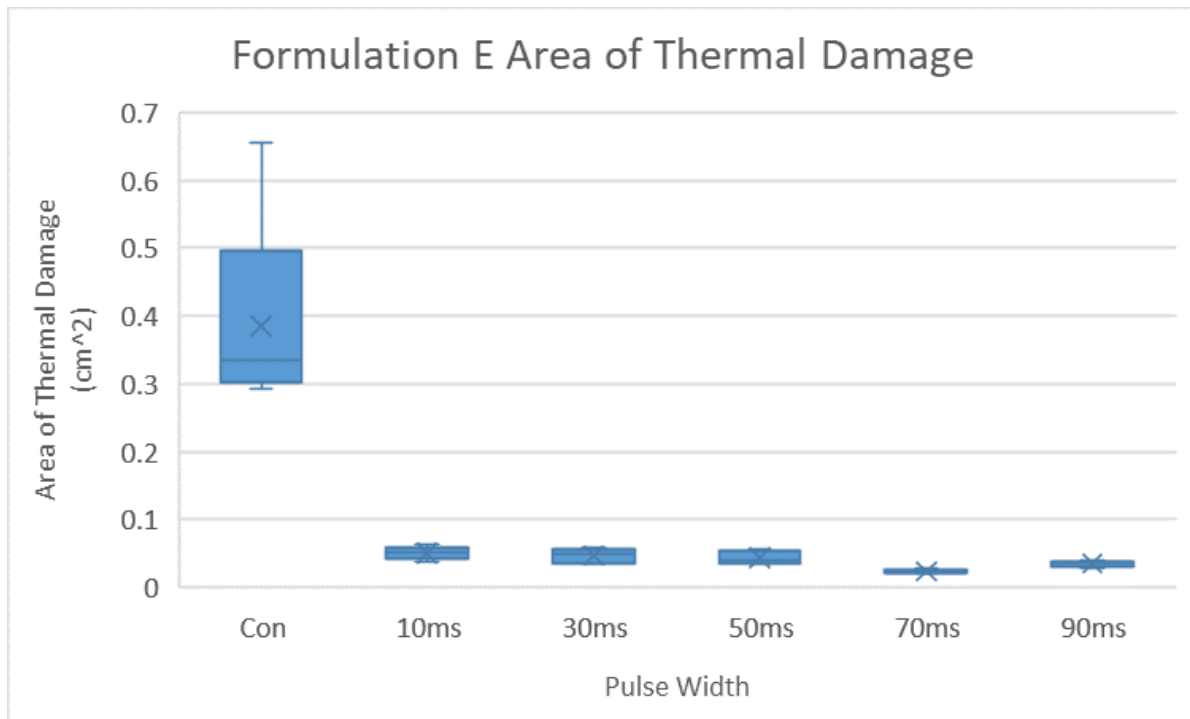


Figure 5.7: Area of Thermal Damage on the Surface of Formulation E Gelatins

Table 5.8: Area (cm<sup>2</sup>) of Present Thermal Damage for Formulation F

	1	2	3	4	5	Median	p-Value
Continuous	0.35	0.283	0.274	0.277	0.323	0.283	-
10 ms	0.183	0.175	0.278	0.17	0.18	0.180	0.032
30 ms	0.172	0.161	0.135	0.209	0.171	0.171	0.008
50 ms	0.124	0.094	0.107	0.083	0.098	0.098	0.008
70 ms	0.028	0.024	0.022	0.02	0.027	0.024	0.008
90 ms	0.039	0.029	0.029	0.029	0.052	0.029	0.008

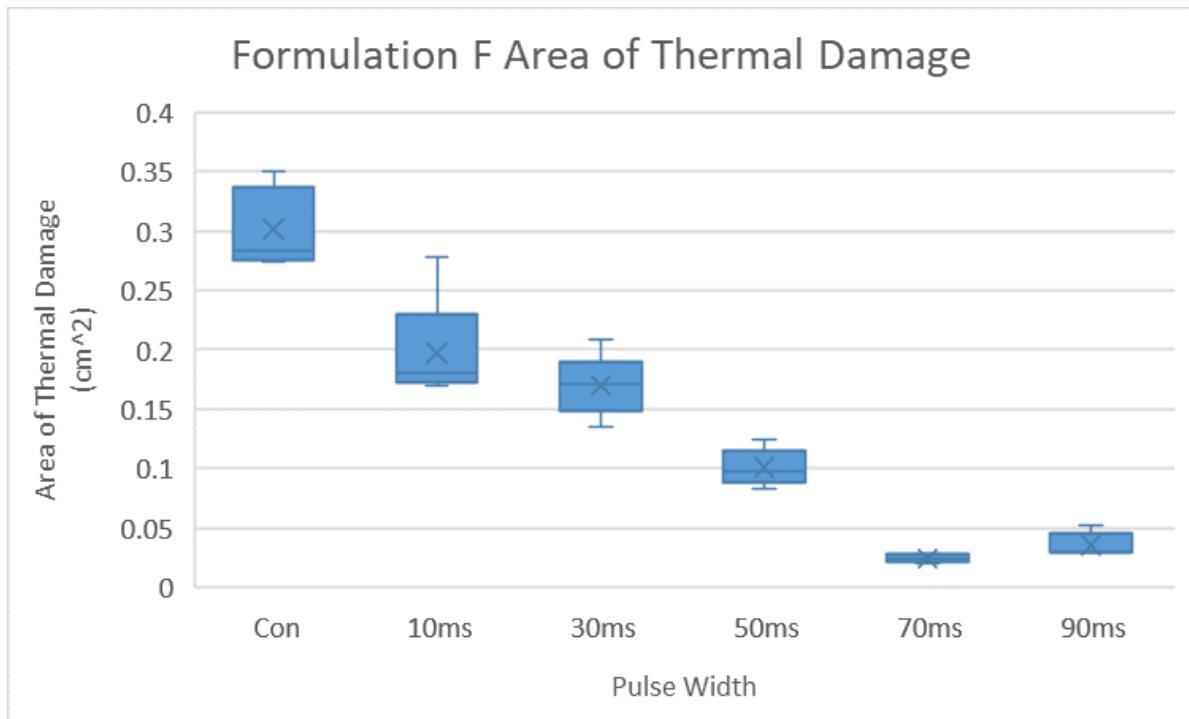


Figure 5.8: Area of Thermal Damage on the Surface of Formulation F Gelatins

Table 5.9: Area (cm<sup>2</sup>) of Present Thermal Damage for Formulation G

	1	2	3	4	5	Median	p-Value
Continuous	0.75	0.259	0.331	0.523	0.542	0.523	-
10 ms	0.031	0.037	0.033	0.044	0.056	0.037	0.008
30 ms	0.035	0.043	0.041	0.032	0.041	0.041	0.008
50 ms	0.016	0.047	0.022	0.034	0.027	0.027	0.008
70 ms	0.012	0.013	0.024	0.018	0.014	0.014	0.008
90 ms	0.018	0.012	0.015	0.019	0.016	0.016	0.008

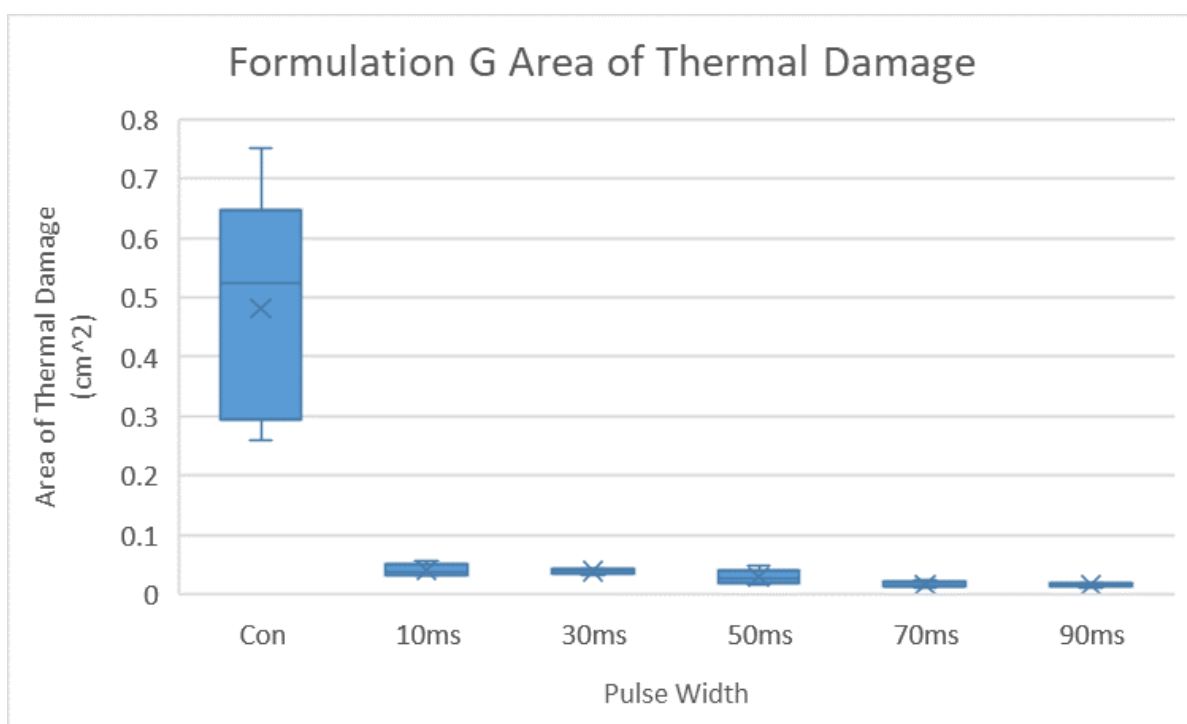


Figure 5.9: Area of Thermal Damage on the Surface of Formulation G Gelatins

#### 5.4 Discussion

From the results above, the pulse width does decrease the overall area of thermal damage. However, the amount of reduction does seem to rely on the concentration of the gelatin mixtures. As stated in the previous section, the lower graded mixtures were closer to liquids than the

higher graded mixtures, which became closer to a solid. The gelatins that were closer to solids had a statistically significant reduction in thermal damage (*i.e.*, compared to continuous illumination) areas than the lower concentrated gelatins. This could provide valuable insight into how various surgical operations might need to be evaluated based on the grade of the cataract.

## Chapter 6: Experimentation on Walnuts

### 6.1 Introduction

To properly prepare for experimentation on human tissue, whether live or cadaver, the device requires testing on various media to examine the efficacy and operation. Now, using a gelatin sample would be a great use of testing the laser to see if the device is functional. However, gelatin samples can liquefy at room temperatures, which could provide mixed results for parameter testing. To find an extraordinary specimen, the culinary world provides experiments with an ordinary ingredient, the walnut.

At first, the walnut may seem like an uneventful object to use as a substitute for experimentation, but upon further examination, the walnut shows itself as a near-identical sample as a cataract if the walnut has a similar absorption and prime scattering coefficient. First, the walnut's thermal and physical properties are almost alike except for the thermal conductivity. These values can be seen in Table 5.1 (Mamani, 2015).

Table 6.1: Comparison of Material Property Values

Property (Units)	Cataract Value	Walnut Values
Density (kg/m <sup>3</sup> )	1000	1123
Thermal Conductivity (W/(m*K))	0.4	0.14
Specific Heat (J/(kg*K))	3000	2779
Absorption Coefficient (1/cm)	10	N/A
Prime Scattering Coefficient (1/cm)	20	N/A

The thermal conductivity could be seen as an issue for the experiments, but the walnut does make up for this with an experimentally found thermal diffusivity that is almost exact to the cataract’s thermal diffusivity (Mamani, 2015). This helps match the critical relaxation times of both the cataract and the walnut with a difference of .04 seconds when assuming similar absorption and prime scattering coefficients. This can be further seen in Table 5.2 (Mamani, 2015).

**Table 6.2: Critical Relaxation Time Comparisons**

Property (Units)	Values from Cataract	Values from Walnut
Penetration Depth (cm)	0.03	0.03
Thermal Diffusivity (cm <sup>2</sup> /s)	0.0013	0.0014
Critical Relaxation Time (s)	0.83	0.79

Judging from these values, the walnut samples would be an excellent substitute for human cataract tissue to test the device’s effectiveness and various laser parameters. By utilizing the walnuts for the experimentation, the goal of these experiments is to help guide the future parameters for operation and provide a physical representation of how the cataract may react under the procedure. Some of the critical aspects of interest for the experiments would be searching for the presence of burn marks, the spread of the burn marks, the sound of any popping, and any darkening from rising oils.

## **6.2 Methods and Materials**

For this experiment series, raw California walnuts in the shell from the company “We Got Nuts” were used. The raw walnuts were used to avoid any interference from substances like sodium or any flavorings used on the nuts. Further, the walnuts within the shell were chosen since the shell provides another layer to keep the walnuts in a fresh state for longer. However, for this experiment, the walnut kernel, or the portion of the walnut that is edible, was the only

portion of the walnut used for the experimentation. For the experiments, the walnuts are cut into five millimeter thick slices, similar to the thickness of the gelatins from the previous chapter.

As for the equipment, the laser mount used in Chapter 4 will be used. This custom-made mount can provide the lasing capabilities that will be discussed further in the experimental procedures. A setup has been made to keep the laser diode stationary to keep the laser focused on one singular point. Also, a camera has been installed near the testing platform to monitor the effects of the laser in real-time.

The laser will be set to 750 milliwatts, like the COMSOL simulations seen in Chapter 3. Then, the pulsing modes would either be set to a continuous mode or a pulsing mode at 10, 30, 50, 70, or 90 milliseconds. The operation of the laser will continue for a total of thirty seconds unless specified otherwise. During the operation, the operator will listen for any popping sounds coming from the walnut. Due to the sound of the connected mount fans, any popping sounds may be masked from the environmental sound pollution. Once the laser operation is completed, the presence and spread of burn marks and any oil rose to the surface will be noted.

As for means of measurement, the present burn marks were measured along the diameter with calipers with a resolution to the hundredth of a centimeter. The diameters were then converted into areas of thermal damage. The samples of the different pulse width sets were individually compared to the continuous pulse set with the Wilcoxon rank-sum test. The pulse width sets were considered statistically different than the continuous set if the corresponding p-values were less than 0.05.

### **6.3 Results and Discussion**

The laser was set to operate at 750 milliwatts. All pulsing widths were able to be tested as they are unaffected by the laser diode model. Because of this issue, the parameters tested,

although not the complete set initially proposed, showed some promise compared to the COMSOL results.

The table of the measured thermal damage is shown below, but the results will be discussed individually. Like the gelatin tables, the data points are divided by trial number and the corresponding pulse width. The median area of thermal damage and the results (p-value) of the Wilcoxon rank-sum test comparing the areas of the pulsed laser trials to the continuous mode operation are shown.

Table 6.3: Area (cm<sup>2</sup>) Measurements of Present Thermal Damage with Laser Power at 750 Milliwatt

Pulse Widths	Trial					Median	p-Value
	1	2	3	4	5		
Continuous	3.05	3.73	2.54	3.56	3.02	3.05	-
10 ms	1.04	0.85	1.04	0.99	0.97	0.99	0.008
30 ms	0.00	0.00	0.00	0.00	0.00	0.00	0.008
50 ms	0.61	0.69	0.52	0.64	0.74	0.64	0.008
70 ms	0.28	0.00	0.00	0.88	0.55	0.28	0.008
90 ms	0.00	0.00	0.00	0.00	0.00	0.00	0.008

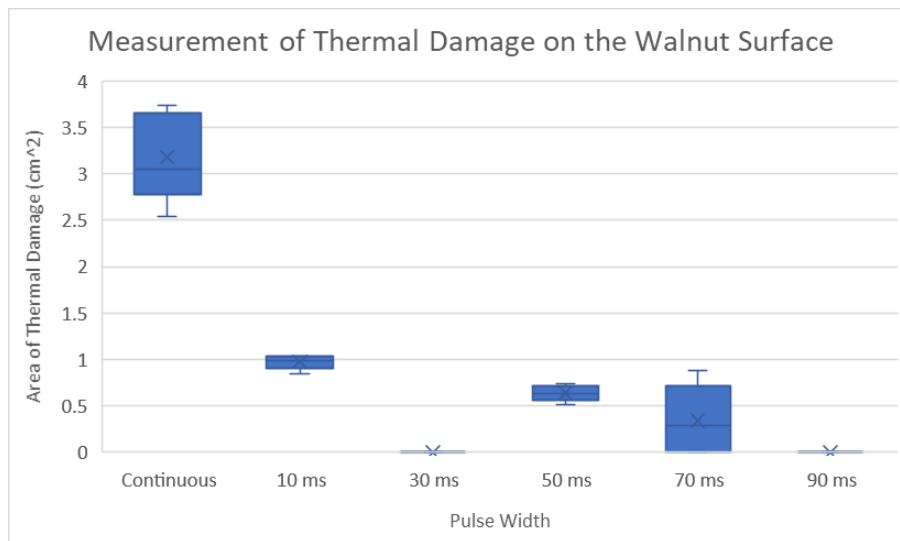


Figure 6.1: Measurements of Thermal Damage on the Walnut Surface at 750 Milliwatts of Power

### 6.3.1 Continuous Mode

During the continuous mode, the walnut almost immediately started on fire. However, the walnuts still provided valuable data. As seen in Table 6.3 and Figure 6.1, the laser left significant, noticeable burn marks on the walnut surface. The reason behind the sizeable thermal damage marks on the surface of the walnuts is due to the dispersion of the heat deposited by the laser. This shows that the COMSOL results showing how the heat was expanded into a larger area was indeed true, and further shows the possible damage that ocular tissues may experience.



Figure 6.2: Photograph of Walnuts After Continuous Lasing

### 6.3.2 Ten Millisecond Pulses

Like the continuous mode, the ten-millisecond pulses resulted in flames but after a more extended period. However, the thermal damage marks on the walnut were more minor on the surface. This is due to the pulse width being lower than the critical relaxation time. When comparing the size of the thermal damage markings to those made during the continuous lasing, the marking diameters in the ten-millisecond pulse ranges were reduced by almost half.



Figure 6.3: Photograph of Walnuts After Ten Milliseconds of Pulsing Width

### 6.3.3 Fifty and Seventy Millisecond Pulses

Unlike the continuous mode and ten-millisecond pulses, the fifty and seventy-millisecond pulse widths did not burn and only left faint marks of thermal damage. The experiment was altered for these test runs to go for five minutes to see if any thermal damage would become apparent. As the comparison of the ten-millisecond pulse marks to the continuous mode marks, the thermal damage marks showed a trend of getting smaller as the pulse widths increased.



Figure 6.4: Photograph of Walnuts After Fifty Milliseconds of Pulsing Width



Figure 6.5: Photograph of Walnuts After Seventy Milliseconds of Pulsing Width

#### 6.3.4 Thirty and Ninety Millisecond Pulses

Interestingly, the thirty and ninety-millisecond pulses did not leave any trace of thermal damage. Although the ninety-millisecond pulse can be explained by the trend of having higher pulse widths result in more minor thermal damage markings, the thirty-millisecond pulse stands out as an anomaly. During the thirty-millisecond pulse experiments, the time was increased to about seven minutes, and no thermal markings were reported. This could be due to an insufficient time to deposit heat, or there could be enough time between pulses to cool.

#### 6.3.5 Discussion of Results

Overall, the experiments show that thermal damage to tissues can be avoided by increasing the pulse width. This is important because the process of phacoemulsification depends on emulsifying the cataract rather than melting or burning away the material. The next step for this experiment would be to submerge the walnut into some water to simulate a hard cataract inside the lens. The goal would be to induce the cavitation within the liquid to create the implosion collapse onto the walnut surface to remove parts of the walnut, resulting in an emulsion of the walnut into the aqueous media.

## **Chapter 7: Conclusion**

As shown from the simulations and the experiments, the new laser-based phacolysis device with microsecond pulses is a viable surgical device. However, there is still more work and experiments left to optimize and test the system thoroughly. The device is still meant to be portable, which means the current large design is not the ideal model for final approval. Also, the device was only tested on walnuts and gelatin phantoms. Although this helps give an accurate idea of what might happen in human tissue, these experiments are not a substitute for performing on an actual cataract.

## **Chapter 8: Future Work**

Although this thesis shows comprehensive work in dealing with preliminary testing, there are still many goals to accomplish. First, an emulsion of one walnut in water and gelatin media would be the final indicator of the overall function of the device. However, due to a shipment of the wrong diodes and the walnuts being harmful to the laser fibers, the experiment had to be postponed due to time. Further, upon completion of the demonstration emulsion, performing an emulsion on a cataract from cadaver tissue will prove the device's functionality. Finally, the device will need to undergo clinical trials before fully becoming useful to medical professionals worldwide.

## References

- Belikov, A. V., Zagorul'ko, A. M., Smirnov, S. N., Sergeev, A. N., Mikhailova, A. A., & Shimko, A. A. (2019). Optical Properties of Human Eye Cataractous Lens in vitro in the Visible and Near-IR Ranges of the Spectrum. *Optics and Spectroscopy*, 574-579.
- COMSOL. (2021). *COMSOL 5.5 Help Handbook*. Stockholm: COMSOL.
- Donaldson, K. E., Braga-Mele, R., Cabot, F., Davidson, R., Dhaliwal, D., Hamilton, R., . . . Yoo, S. H. (2013). Femtosecond laser-assisted cataract surgery. *Journal of Cataract & Refractive Surgery*, 1753-1763.
- Erie, J. C., Hodge, D. O., & Mahr, M. A. (2020). Long-term trends and stabilization of cataract surgery rates: a population-based study. *Journal of Cataract & Refractive Surgery*, 1056-1057.
- Farrer, A. I., Odeen, H., de Bever, J., Coats, B., Parker, D. L., Payne, A., & Christensen, D. A. (2015). Characterization and evaluation of tissue-mimicking gelatin phantoms for use with MRgFUS. *Journal of Therapeutic Ultrasound*.
- Fisher, R. F. (1969). Elastic constants of the human lens capsule. *Journal of Physiology*, 1-19.
- Henriquez, M. A., Mejias, J. A., Rincon, M., Izquierdo Jr., L., & Binder, P. S. (2019). Correlation between lens thickness and lens density in patients with mild to moderate cataracts. *British Journal of Ophthalmology*.
- Incropera, F. P., & Dewitt, D. P. (2011). *Fundamentals of Heat and Mass Transfer*. Hoboken: John Wiley & Sons.
- Jacques, S. L. (1992). How tissue optics affect dosimetry for photochemical, photothermal, and photomechanical mechanisms of laser-tissue interaction. *Proceedings of SPIE* (pp. 316-322). New York: SPIE.
- Lee, R., Kasuga, T., Cui, Q., Porco, T., Huang, G., He, M., & Lin, S. (2014). Association between Baseline Iris Thickness and Prophylactic Laser Peripheral Iridotomy Outcomes in Primary Angle-Closure Suspects. *Ophthalmology*, 1194-1202.
- Liou, H.-L., & Brennan, N. A. (1997). Anatomically accurate, finite model eye. *Journal of the Optical Society of America*, 1684-1695.
- Liu, Y.-C., Wilkins, M., Kim, T., Malyugin, B., & Mehta, J. S. (2017). Cataracts. *The Lancet*, 600-612.

- Mamani, I. (2015). Modeling of Thermal Properties of Persian Walnut Kernel as a Function of Moisture Content and Temperature Using Response Surface Methodology. *Journal of Food Processing and Preservation*, 2762-2772.
- Mirnezami, S. A., Jafarabadi, M. R., & Abrishami, M. (2013). Temperature Distribution Simulation of the Human Eye Exposed to Laser Radiation. *Journal of Lasers in Medical Sciences*, 175-181.
- Mirnezami, S. A., Jafarabadi, M. R., & Abrishami, M. (2013). Temperature Distribution Simulation of the Human Eye Exposed to Laser Radiation. *Journal of Lasers in Medical Sciences*, 175-181.
- Ooi, E.-H., & Ng, E. Y.-K. (2008). Simulation of aqueous humor hydrodynamics in human eye heat transfer. *Computers in Biology and Medicine*, 252-262.
- Pescosolido, N., Barbato, A., Giannotti, R., Komaiha, C., & Lenarduzzi, F. (2016). Age-related changes in the kinetics of human lenses: prevention of the cataract. *International Journal of Ophthalmology*, 1506–1517.
- Ruit, S., Tabin, G. C., Nissman, S. A., Paudyal, G., & Gurung, R. (1999). Low-cost high-volume extracapsular cataract extraction with posterior chamber intraocular lens implantation in Nepal. *Ophthalmology*, 1887-1892.
- Ruru, D., Yingqing, H., Yan, Q., Qidong, C., & Lei, C. (2012). Measuring pure water absorption coefficient in the near-infrared. *Journal of Remote Sensing*, 192-206.
- Shahbazi, S., Studnicki, J., & Warner-Hillard, C. W. (2015). A Cross-Sectional Retrospective Analysis of the Racial and Geographic Variations in Cataract Surger. *PLOS ONE*.
- Sun, H., Han, M., Niemz, M. H., & Bille, J. F. (2007). Femtosecond Laser Corneal Ablation Threshold: Dependence on Tissue Depth and Laser Pulse Width. *Lasers in Surgery and Medicine*, 654-658.
- Tan, L. (2006). Increasing the volume of cataract surgery: an experience in rural China. *Community Eye Health Journal*, 61-63.
- van den Berg, T. J., & Spekreijse, H. (249-253). Near Infrared Light Absorption in the Human Eye Media. *Vision Research*, 1997.
- Wirbelauer, C., Koop, N., Tuengler, A., Geerling, G., Birngruber, R., Laqua, H., & Brinkmann, R. (2000). Corneal Endothelial Cell Damage After Experimental Diode Laser Thermal Keratoplasty. *Journal of Refractive Surgery*.
- Zacharias, J. (2008). Role of cavitation in the phacoemulsification process. *Journal of Cataract & Refractive Surgery*, 849-852.